Effects of bed discordance on flow, turbulence, and mixing at an idealized asymmetrical confluence between two shallow streams

Chenyu Jiang [1,2,3] and George Constantinescu [2]

[1] *Water Conservancy Development Research Center of Taihu Basin Authority, Shanghai 200438, China*

[2] *Department of Civil and Environmental Engineering and IIHR-Hydroscience and Engineering, The University of Iowa, Iowa City, Iowa 52240, USA*

[3] *Key Laboratory of Hydrologic-cycle and Hydrodynamic System of Ministry of Water Resources, Hohai University, Nanjing, Jiangsu 210098, China*

(Received 1 September 2025; accepted 22 April 2026; published 11 May 2026)

When two streams of equal densities but of unequal velocities and different flow directions come into contact, large-scale coherent structures are generated downstream of the confluence apex. They include vertical vortices inside the region of high mean shear between the fluids originating in the two tributaries [i.e., the mixing interface (MI)] and streamwise-oriented-vortical (SOV) cells inside and in the vicinity of the MI. The flow physics becomes even more complex when the bed elevations of the tributary channels are not the same as that of the downstream channel. Eddy resolving simulations are used to investigate how the gradual increase in the level of bed discordance between the minor tributary channel and the main downstream channel affect flow, turbulence structure, sediment entrainment mechanisms and mixing at an asymmetrical confluence with a confluence angle of 70°. To better isolate the effects of bed discordance, simulations are performed with idealized conditions in which the bottom surfaces of the open channels are horizontal except near the region where the minor tributary connects with the main channel. The other main flow parameter that is varied is the discharge ratio between the two streams, QR. Results show that for constant QR, the coherence of the vertical MI vortices increases with increasing bed discordance, and the wake mode becomes gradually dominant even though the velocity and momentum ratios are not close to unity. Increasing the bed discordance reduces the coherence and number of SOV cells forming on the minor tributary side of the MI and promotes the formation of a near-bed intrusion of mixed fluid into the minor tributary side of the main channel near the confluence apex. This is the main mechanism that is responsible for the increase in the rates of mixing between the two streams with increasing bed discordance for constant QR. While for small bed discordance levels, sediment entrainment inside the confluence hydrodynamic zone is driven primarily by the SOV cells, for sufficiently large bed discordance levels and QR, sediment entrainment on the minor tributary side is mainly driven by the plunging core of high free surface velocities as it enters the main channel.

DOI: 10.1103/lpm8-kht7

I. INTRODUCTION

Understanding the flow structure at open channel confluences and its effect on mixing is of particular importance for geophysical systems given that confluences play an important role in riverine systems and riverine ecology [1–3]. Moreover, erosion is significantly enhanced inside the confluence hydrodynamics zone where large-scale turbulence is generated due to the interaction between the converging flows from the two tributaries and the changes in the planform geometry and bathymetry around the location where the two streams join [4,5]. The main parameters that affect hydrodynamics and transport downstream of the confluence apex are the planform geometry, the momentum and velocity ratios of the flow in the incoming tributaries upstream of the confluence apex, the density contrast between the two streams, and the level of bed discordance between the channel beds in the two tributaries [6,7]. The main variables describing the planform geometry are the angles α_1 and α_2 between the centerlines of the two tributary channels and the centerline of the main channel downstream of the confluence apex. Based on the values of these angles, confluences are classified as symmetrical ($\alpha_1 = \alpha_2$) or asymmetrical. The confluence angle is $\alpha = \alpha_1 + \alpha_2$.

A. Main types of coherent structures generated at confluences

Assuming the density difference between the incoming streams is negligible, the main types of coherent structures generated downstream of the confluence apex include: (1) vertical vortices inside the mixing interface (MI) region, and (2) streamwise-oriented-vortical (SOV) cells close to the boundaries of the MI at confluences with a sufficiently large confluence angle. The MI vortices and SOV cells play an important role in mixing as they enhance transverse turbulent diffusion and transverse advective dispersion, respectively [8]. In most cases, the shear layers on the two sides of the confluence apex separate and shed vortical tubes. As a result of the interactions between the separated shear layers, a small wake, or stagnation zone, forms in the immediate vicinity of the junction apex.

Constantinescu *et al.* [9,10] were the first to make the distinction between two types of MIs that can form at concordant confluences with no density contrast. Generally, these types are a function of the momentum ratio $\text{MR} = (\rho g Q_2 U_2)/(\rho g Q_1 U_1)$, discharge ratio $\text{QR} = Q_2/Q_1$, and the velocity ratio $\text{VR} = U_2/U_1$, between the two tributaries, where ρ is the density, g is the gravitational acceleration, Q is the discharge, and U is the bulk channel velocity in the tributary. The subscripts 1 and 2 denote the variables in the major and minor tributaries, respectively. If these ratios are much smaller or much larger than one, then the MI contains corotating vortices generated via the Kelvin-Helmholtz (KH) instability. Similar to a standard deep mixing layer [11], the KH vortices undergo vortex pairing. The MI is classified as being in the KH mode. However, if MR, QR, and VR are close to unity near the junction apex, then the MI is likely to contain counterrotating vortices whose mechanism of formation is similar to that of billow vortices forming in the wake of a bluff body. For such cases, the MI is classified as being in the wake mode. Depending on the planform geometry, bathymetry and flow conditions, the two modes can coexist. For such cases, the MI contains counterrotating vertical vortices but the coherence of the vortices rotating in one direction is significantly larger than the one of the vortices rotating in the opposite direction (e.g., Ref. [12]). Generally, the formation of a large stagnation zone favors the presence of a strong wake mode.

The presence of the bed significantly affects the dynamics of the vertical MI vortices at large distances from the confluence apex. As the size of their cores becomes larger than the flow depth, the dynamics of the MI vortices is strongly influenced by the presence of the bed surface [13–15]. As opposed to a deep mixing layer, the rate of growth of the MI width decreases away from its origin and becomes negligible once the vertical vortices start losing their coherence because of their interaction with the bed surface [15–19]. Another important bed friction effect is that vortex pairing ceases for MIs in the KH mode at sufficiently large distances from the confluence apex. The suppression of vortex pairing and reduction in the coherence of the MI vortices corresponds to the start of the transition to what is called the equilibrium regime in which the MI contains only smaller-scale turbulence generated via stretching of the vertical MI vortices present in the near field [19].

Vortical structures called SOV cells form at angled confluences because the two streams lose their transverse momentum as they change their direction downstream of the confluence apex [7,20]. The

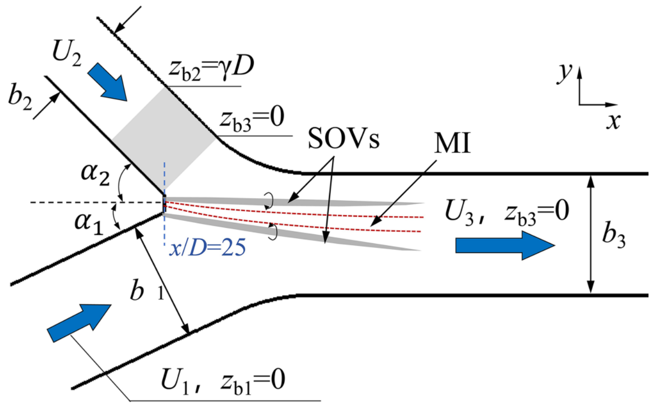

FIG. 1. Sketch showing planform geometry of the asymmetrical confluence ($\alpha_1 = 25°$, $\alpha_2 = 45°$), the bed elevations (z_{b1},z_{b2}, z_{b3}), the channel widths (b_1, b_2, b_3), and the cross-sectional mean flow velocities (U_1, U_2, U_3) in the open channels. The bed discordance height for the minor tributary channel is γD with $0 \leqslant \gamma \leqslant 0.5$. Also shown are the mixing interface (MI) between the two incoming streams and the SOV cells forming in the vicinity of the MI.

free surface elevation increases inside the MI in the region where the high-velocity cores from the two tributaries come into contact. A secondary flow is generated inside the MI along the vertical direction. As this secondary flow reaches the bed, it is diverted away from the MI and then raises back toward the free surface to form SOV cells [9,19,21]. Secondary corotating SOV cells may form on one or both sides of the MI [9,10,21], similarly to secondary horseshoe vortices in junction flows [22]. Finally, the cores of the most coherent SOV cells can be subject to aperiodic bimodal oscillations [10,21] which explains the large erosive capacity of these vortices.

The change in the direction of the incoming streams at angled confluences may generate cells of secondary flow on one or both sides of the MI [23]. These cells of secondary flow may increase, or decrease, the coherence of the SOV cells, depending on their sense of rotation with respect to that of the SOV cell. Finally, bed discordance may also induce cells of secondary flow downstream of the confluence apex [24].

B. Proposed approach to investigate bed discordance effects

Of particular interest for natural river confluences is the case of discordant confluences with a large difference of the flow depths in the two tributaries (i.e., larger than 15%). Discordant confluences often form when a smaller river (i.e., generally a tributary with a smaller discharge, flow depth, and cross section) joins a larger one. Most often, the smaller tributary makes a larger angle (α_2) with the downstream channel compared to the one (α_1) between the larger tributary and the downstream channel. In such cases, the increased three-dimensionality of the flow near the confluence apex often induces large changes in flow patterns and the large-scale turbulent structures which, in turn, affect mixing [25–29]. Despite many experimental (e.g., Refs. [6,24,25,27,29–35]) and several numerical studies using eddy-resolving simulations (e.g., Refs. [36–40]) conducted at discordant confluences, there are still important knowledge gaps in terms of understanding how increasing bed discordance affects flow, turbulence structure, and, ultimately, transport and mixing.

Given the additional complexity of the flow at natural confluences characterized by complex bathymetry and irregular bank lines, it is suitable to reduce the number of flow variables characterizing the planform geometry and bathymetry to better understand the effects associated with varying the degree of bed discordance. This is why the present study considers a simplified planform geometry in which two straight tributary channels of widths b_1 and b_2 merge into a straight channel of width b_3 (Fig. 1). The channel Froude numbers are assumed to be small such that the free surface is horizontal. Given that the aspect ratio of most cross sections of river channels is between 15 and 25, the width to depth ratio of the confluence channels is at least 15 for the simplified geometry confluence.

The present paper uses a similar approach to that of Cheng and Constantinescu (21) by performing a series of numerical experiments of flow and mixing at an asymmetrical confluence ($\alpha_1 = 25^\circ$, $\alpha = 70^\circ$) in which the flow depth of the smaller tributary can be up to 50% smaller than those of the larger tributary and the main channel. A constant slope ramp ending at the confluence apex is used inside the smaller tributary to mimic the gradual change in the bed elevation observed at many confluences where a smaller tributary joins a larger one. This type of simplified approach was already used for concordant confluences (i.e., confluences with $D_1 = D_2 = D_3$ where the index 3 is used for the main channel variables) to study effect of planform geometry (e.g., α_1, α_2, α) and velocity ratio on the structure and spatial development of the MI between parallel (i.e., $\alpha = 0^\circ$, see Ref. [19]) and nonparallel incoming streams [21]. The aspect ratio of the downstream channel was larger than 50 such that the turbulent eddies generated in the region where the banks changed orientation did not get close to the MI. These studies provided a full picture of the spatial development of a shallow mixing layer during the early and later stages of the transition to the equilibrium regime. These results are relevant for the present study as a concordant confluence corresponds to the limiting case of zero bed discordance.

C. Research gaps and objectives

Though many field studies were conducted for confluences with a high degree of bed discordance, it is still not clear what is the exact effect of bed discordance on the flow structure, mixing and entrainment. This is because natural confluences, and discordant confluences in particular, are generally characterized by very complex bathymetries that, besides the confluence scour hole, may contain sediment bars and other large-scale morphological features, irregular bank lines with limited regions of high curvature, and a main channel containing regions of high curvature, as most river channels are meandering. Most laboratory studies of flow at discordant confluences conducted with simplified channel planform geometries (e.g., Refs. [33,41]) also considered sediment transport and focused on flow patterns at equilibrium conditions. Relatively little quantitative information was provided on the three-dimensional (3D) flow and turbulence structure. Numerical studies conducted with simplified planform geometry (e.g., Ref. [36]) also focused on cases with a naturally deformed bed but did not investigate in a systematic way bed discordance effects.

Of particular interest is to gain fundamental insight on how confluence hydrodynamics, coherent structures and mixing respond to changes in the level of bed discordance and momentum ratio. Maybe the most controversial topic is related to the effect of bed discordance on SOV cells given that several field studies (e.g., Refs. [25,33,42]), and numerical studies (e.g., Refs. [36–38],) reported no evidence of SOV cells at confluences with natural bathymetry characterized by a high degree of bed discordance (i.e., confluences with a ratio of the flow depths in the incoming channels close to 0.5). The main goals of the present paper are to understand how the gradual increase of the bed elevation difference between the two tributaries affects:

(a) the structure of MI (i.e., the coherence of the vertical vortices, dominant mode) and its spatial development away from the confluence apex (i.e., width, centerline position),

(b) the formation, position, and dynamics of SOV cells on the two sides of the MI,

(c) sediment entrainment mechanisms and the overall sediment entrainment capacity of the flow inside the main channel,

(d) mixing and the capacity of coherent structures to enhance mixing.

Given that the effect of bed discordance is best revealed by maintaining constant the discharges in the two tributaries and gradually increasing the bed elevation of the minor tributary away from the confluence apex, the present paper also investigates if the effect of the bed discordance on the aforementioned flow phenomena and coherent structures is qualitatively similar at confluences with two different values of QR, or equivalently, two different values of the momentum ratio at the confluence apex, $\mathrm{MR}_{\mathrm{apex}}$, calculated with the cross-section-averaged velocities near the confluence apex, where the flow depths in the three channels are always equal.

II. TEST CASES AND NUMERICAL METHOD

Given that the focus of this paper is on the case when a small tributary joins a large river (i.e., $Q_2 < Q_1$), it is of interest to consider a simplified geometry where the main geometrical parameters (e.g., widths b_1, b_2 and b_3 and flow depths D_1, D_2, D_3 of the channels forming the confluence, confluence angles α_1 and α_2) and associated flow conditions (e.g., discharge ratio) are representative of such situations. Given that eddy resolving simulations require large amounts of computational resources, the number of test cases that can be considered is limited and exploring all combinations in terms of the main geometrical and flow variables controlling flow and mixing at the confluence is not possible. Following the work of Refs. [43, 44], optimality concepts can be applied to determine the appropriate combinations of the main flow and geometrical variables that represent a wide range of natural conditions at discordant confluences between a larger and a smaller tributary. The concepts relay on minimization of the stream power and on the relation between the channel width, b, and the formative discharge, Q (i.e., $b \sim Q^{1/2}$) in natural open channels. These concepts allow determining the angles between the two tributary channels and the downstream channel as a function of the discharge ratio (i.e., $\cos(\alpha_1) = (1 + Q_2/Q_1)^{\beta}$ and $\cos(\alpha_2) = (1 + Q_1/Q_2)^{\beta}$). The range of the exponent β varies from -0.2 to -1.0 [43], but values at most natural confluences are generally close to -0.3. So, as Q_2/Q_1 decreases, α_2 increases and α_1 decreases, meaning the main tributary becomes more aligned with the main channel. Moreover, the confluence angle $\alpha = \alpha_1 + \alpha_2$ is related to the degree of asymmetry of the confluence. Assuming $\beta = -0.3$, α decreases from 60° for $Q_2/Q_1 = 1$, which also implies $b_2/b_1 = 1$ and a width of the downstream channel $b_3 \approx 1.4b_1$ (symmetric confluence), to 90° for $Q_2/Q_1 \ll 1$ (highly asymmetric confluence), which also implies $\alpha_1 \approx 0°$, $\alpha_2 \approx 90°$, $b_3 = b_1$, and $b_1/b_2 = (Q_1/Q_2)^{1/2}$. Most confluences will be asymmetric with intermediate configurations and discharge ratios. A value of $Q_2/Q_1 = 0.4$ is close to typical values at many natural confluences. In this case, $\alpha_1 \approx 25°$, $\alpha_2 \approx 45°$, $b_2 \approx 0.63b_1$, $b_3 \approx 1.15b_1$ and $\mathrm{MR}_{\mathrm{apex}} \approx 0.22$. As explained below, simulations were performed with two different values of $\mathrm{MR}_{\mathrm{apex}}$. The main geometrical dimensions of the confluence in the simulations were $\alpha_1 = 25°$, $\alpha_2 = 45°$, $\alpha = 70°$, $b_3 = 25\,D$, $b_1 = 22.7\,D$, and $b_2 = 0.65b_1 = 14.8\,D$.

Field studies typically reported maximum bed slope values of about 25° in the region where the minor tributary connects to the main channel [32]. Assuming a maximum discordance height of 50% of the flow depth in the main channel, the length of the constant length ramp introduced at the downstream end of the minor tributary is close to $1.2D_3$. In the present study $D_1 = D_3 = D$ and $0.5D \leqslant D_2 \leqslant D$, where $D = D_3$ is generally used as the length scale when analyzing results in nondimensional form. As the beds of the three channels are horizontal except for the ramp region, and the free surface is also horizontal, the elevation of bed inside the major tributary and the main channel is $z_b = 0$, while that of the free surface is $z_{\mathrm{FS}} = D$. The bed elevation inside the minor tributary away from the ramp, z_{b2}, varies between $0.0D$ (concordant bed cases) and $0.5D$ (Table I). For all cases, the variation in the bed elevation inside the minor tributary is such that the flow depth reaches D at the downstream section of the minor tributary (i.e., at the confluence apex). The lateral walls of the channels are vertical. The two bank lines contain a low curvature region ($R = 27\,D$) connecting the straight parts (Fig. 1). The distance from the confluence apex to the downstream section is $200D$. The lengths of the tributary channels are close to $40D$. The cross section containing the apex corresponds to $x/D = 25$. The left and right banks of the downstream channel are defined with respect to the direction of the flow.

The effects of varying the bed discordance level are investigated in two series of simulations conducted with constant values of the discharges in the two tributaries. The values of Q_1 and Q_2 are different in the two series of simulations, but the main channel discharge, Q_3, and bulk velocity, $U_3 = Q_3/(b_3D)$, are the same. As a result, the discharge ratio, QR, or equivalently the momentum ratio near the confluence apex, $\mathrm{MR}_{\mathrm{apex}}$, are fixed in each series of simulations. The first series

TABLE I. Main flow and geometrical parameters in the test cases.

	Case 1	Case 2	Case 3	Case 4	Case 5
z_{b2}/D	0	0.25	0.5	0	0.5
z_{FS}/D	1	1	1	1	1
QR	0.36	0.36	0.36	0.57	0.57
VR	0.55	0.74	1.1	0.88	1.75
MR	0.2	0.27	0.4	0.5	1.0
$V\text{R}_{\text{apex}}$	0.55	0.55	0.55	0.88	0.88
MR_{apex}	0.2	0.2	0.2	0.5	0.5

of simulations are conducted with QR $= 0.36$, $\text{MR}_{\text{apex}} = 0.2$, and $z_{b2}/D = 0$, 0.25, and 0.5. The second series of simulations are conducted with QR $= 0.57$, $\text{MR}_{\text{apex}} = 0.5$, and $z_{b2}/D = 0$ and 0.5. Also included in Table I is the velocity ratio calculated with the mean cross-sectional velocity at the downstream end of the two tributaries, $V\text{R}_{\text{apex}}$. The mean velocity inside the main channel, U_3, which is the same in all cases, is chosen as the velocity scale (i.e., $U = U_3$).

The Reynolds number, $\text{Re} = UD/\nu$ (ν is the kinematic viscosity) is equal to 12 000, which is sufficient to ensure that the channel Reynolds numbers in the two tributaries are at least 6000. The Reynolds number is very close to the value (Re $= 15\,000$) used in the simulations of Refs. [19,21]. Assuming $D = 0.08$ m and $U = 0.15$ m/s, the Froude number is close to 0.17. One difference with the aforementioned studies is the smallest aspect ratio of the confluence channels. In particular, the aspect ratio of the main channel in the concordant bed simulations of Cheng and Constantinescu [21] was close to $50D$, which is much larger than typical values for natural streams. This was done to allow studying the spatial development and structure of a MI over large distances without any disturbances induced by flow features (e.g., shear layers) and eddies generated at the banks. Given that the aspect ratios of the confluence channels in the present simulations are within the range of values observed at natural confluences, such interactions are expected to be present.

The simulations are performed using the delayed version of detached eddy simulation (DES) which is a large-eddy-simulation (LES)-based technique largely used for river engineering applications [45]. DES is often described as a hybrid method blending Reynolds-averaged Navier Stokes (RANS) with LES. This is because the turbulence length scale in DES is modified such that the turbulence length scale away from solid surfaces becomes proportional with the local grid spacing, as in classical LES. The numerical approach is the same as the one used in the related studies conducted by Cheng and Constantinescu [19,21] for concordant confluences. The Spalart-Allmaras (SA) model is used as the base RANS model [46]. The incompressible Navier-Stokes equations are integrated using a fully implicit, fractional-step method. An advection-diffusion equation is solved for the passive scalar used to track the mixing between the two streams. The molecular Prandtl number is equal to 6. The DES eddy viscosity is used to estimate the eddy diffusivity assuming a unity turbulent Prandtl number. The governing equations are formulated in generalized curvilinear coordinates on a nonstaggered grid. A boundary fitted mesh is used to discretize the governing equations. The convective terms in the momentum equations are discretized using a blend between the fifth-order-accurate, upwind-biased scheme and the second-order central scheme. All the other terms in the momentum and pressure-Poisson equations are approximated using second-order central differences. The discrete momentum (predictor step), scalar transport and turbulence model equations are integrated in pseudo-time using the alternate direction implicit approximate factorization scheme. Time integration is done using a double time-stepping algorithm. The time discretization is second-order accurate. The code is parallelized using message-passing interface.

The present model was extensively validated to predict flow and mixing at confluences with simplified and naturally deformed bathymetry. In the case of a zero-angle concordant confluence between two streams of different velocities but of same density, Cheng and Constantinescu [19] found very good agreement between the numerical predictions and the experimental data for the shallow mixing layer forming in a wide, constant-depth channel. The extensive measurements of velocity, mean temperature and turbulent kinetic energy performed at a small concordant confluence by Refs. [42,47] were used to validate the solver for high angle confluences with negligible density contrast between the incoming streams (see Refs. [9,10,48]). For discordant bed confluences, comparison of predicted flow patterns with those observed in laboratory experiments is discussed by Guillem-Ludena *et al.* [36]. Validation of the passive scalar transport module of the code is discussed by Chang *et al.* [49].

In the present simulations, the bed and sidewall surfaces of the confluence channels were modelled as no-slip, smooth walls. Given that this study focuses on low Froude number confluent flows, the free surface was modeled as a shear-free, rigid-lid boundary as in the related numerical investigations of Constantinescu *et al.* [19,21]. Precursor simulations were used to calculate the fully developed turbulent flow at the two inlet sections of the tributary channels. A convective boundary condition was used at the outlet for all variables. This type of exit boundary condition is commonly used for both DES and LES simulations [46]. A unity value of the scalar concentration, C, was specified at the inlet of the major tributary, while C was set equal to zero at the inlet of the minor tributary. The normal gradient of C was set to zero at the free surface and at the wall boundaries. The molecular Schmidt number was equal to one.

The mesh topology and level of mesh refinement were very similar to those used in the concordant confluence simulations performed by Cheng and Constantinescu [19] at similar Reynolds numbers. Each horizontal plane contained close to 0.7 million grid points, while 36 points were used in between the channel bed and the free surface. For all solid surfaces, the grid spacing in the wall normal direction corresponded to around one wall unit such that the use of wall functions was avoided. Near the free surface, the vertical grid spacing was close to $0.03D$ corresponding to about 18 wall units. The average cell size in the horizontal directions was close to 100 wall units. The time step was $0.005D/U$. Results are discussed after the numerical solutions became statistically steady, around $800D/U$ after the start of the simulations. Statistics were calculated over the next $1000D/U$.

III. DYNAMICS OF COHERENT STRUCTURES INSIDE AND AROUND THE MIXING INTERFACE

A. Mixing interface

In all simulations conducted with $\mathrm{QR} = 0.36$, the momentum ratio is less than 0.4. This would suggest that the MI is in the KH mode in these cases. However, analysis of the vertical vorticity fields in Figs. 2(a)–2(c) shows that this is not exactly the case. Though the MI contains only patches of vorticity of the same sign in the concordant bed simulation (Case 1), the KH mode is weak with large corotating vortices forming only far from the confluence apex [i.e., for $x/D > 65$, see Fig. 2(a)]. The upstream part of the MI resembles more to a disturbed vorticity sheet containing elongated patches of vorticity aligned with the streamwise direction. The fact that the KH mode is weak is due to the strong acceleration of the flow from the minor tributary as it changes direction downstream of the confluence apex and to the formation of a high-vorticity shear layer at the left bank that constrains the flow originating in the minor tributary and further accelerates it as it moves into the main channel. The strength of the KH mode is directly proportional to the mean shear across the MI. Though the velocity ratio calculated with the bulk velocities in the two tributaries is much less than one (i.e., $\mathrm{VR} = 0.55$), its values calculated at streamwise locations situated downstream of the confluence apex (i.e., $x/D > 25$) are much closer to unity. This explains the relative weakness of the KH mode even though MR and QR are not close to one.

Results for Case 2 [Fig. 2(b)] show that for a moderate level of the bed discordance (i.e., $z_{b2}/D = 0.25\,D$), both the KH mode and wake mode are present as the MI contains vertical vortices with positive and negative vertical vorticity inside their cores, but the circulation of the vortices containing positive vertical vorticity is larger. The presence of the wake mode is facilitated by the

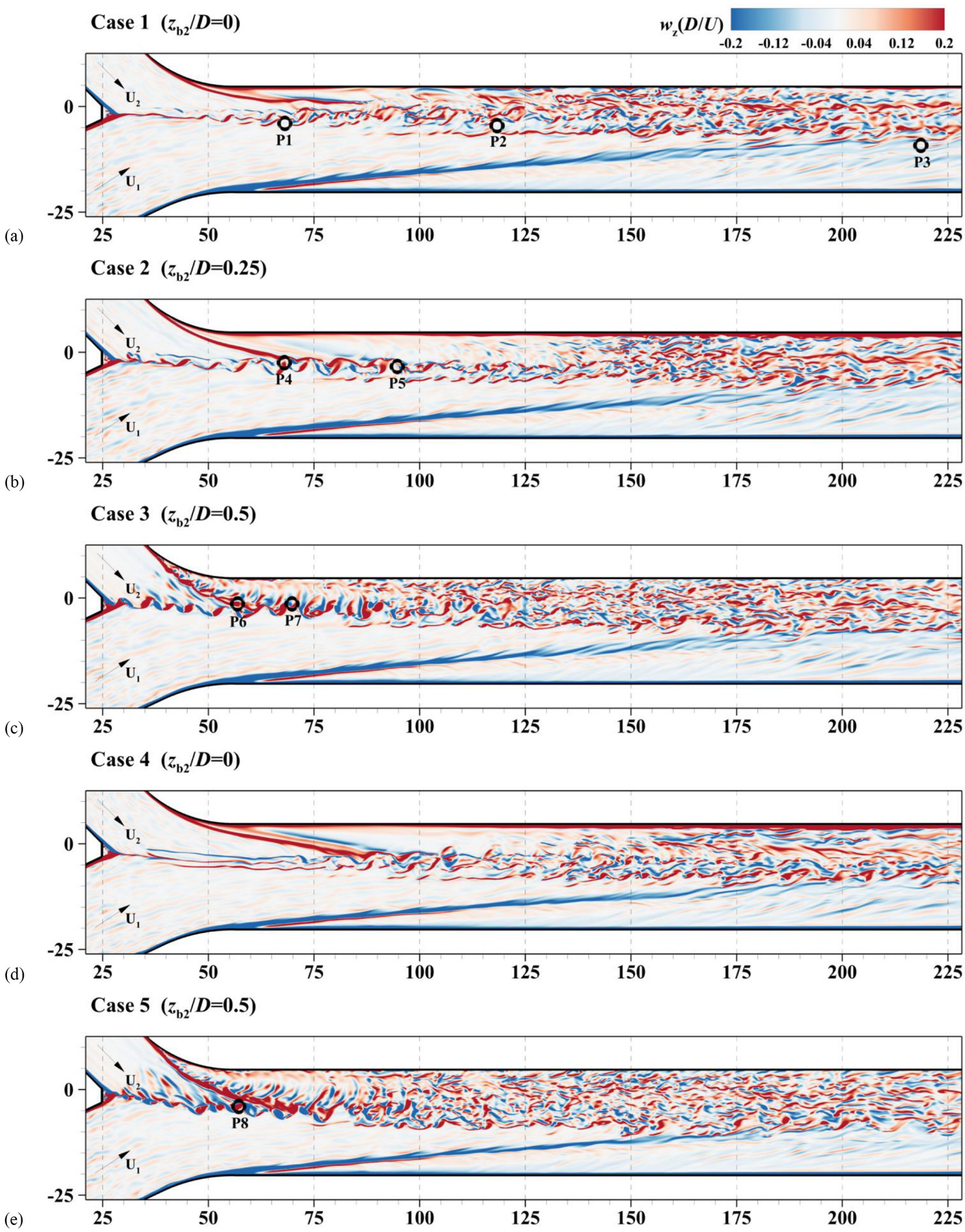

FIG. 2. Instantaneous vertical vorticity, $\omega_z D/U$ close to the free surface ($z/D = 0.9$). (a) Case 1; (b) Case 2; (c) Case 3; (d) Case 4; (e) Case 5.

formation of a stagnation zone (i.e., small recirculation zone starting at the confluence apex that is bordered by the separated shear layers on the two sides of the confluence apex) in all cases. What is also interesting is that at a given distance from the confluence apex, the circulation of the MI vortices is, on average, larger in Case 2 compared to Case 1. As the bed discordance is further increased to $0.5D$ in Case 3, the wake mode becomes dominant [Fig. 2(c)]. The separated shear layers are characterized by strong interactions that lead to the formation of highly coherent counterrotating vortices starting near the confluence apex.

So, in the simulations conducted with $\mathrm{QR} = 0.36$, the increase of the bed discordance strengthens the wake mode and weakens the KH mode. This is also true for the simulations conducted with $\mathrm{QR} = 0.57$ where the wake mode is clearly the dominant one in Case 5 [Fig. 2(e)], while being absent in the corresponding concordant bed simulation [Case 4, Fig. 2(d)]. What is interesting is that the MI does not contain strongly coherent vertical vortices in Case 4 where the KH mode is weak even though $\mathrm{MR} = 0.5$ and $\mathrm{QR} = 0.57$. Though a stagnation zone also forms in Case 4, the separated shear layers on the two sides of the confluence apex are close to steady and no vortices are shed.

The other main feature of the vertical vorticity fields in Fig. 2 is the presence of strong shear layers forming at the two banks in the region where the bank lines are curved. These shear layers separate the core of high velocities associated with the tributary from much slower fluid moving close to the banks. In some cases, flow separation is observed in between the shear layer and the corresponding bank line. Both separated shear layers penetrate until the MI, with the one originating at the left bank (minor tributary side) reaching the MI first (Fig. 2). In particular, strong interactions are present between the MI vortices and the eddies shed from the downstream end of this shear layer. Such interactions are commonly observed at natural river confluences (e.g., Refs. [9,10]). These interactions together with the smaller-scale turbulence generated between the MI and the left bank, downstream of the location where the shear layer reaches the MI, induce strong stretching of the vertical vortices generated over the upstream part of the MI. For the most part, these vortices lose their coherence around $x/D = 100$. The main effect of increasing the bed discordance is to reduce the streamwise distance where the shear layers originating at the banks reach the MI. For example, the left side shear layer starts interacting with the MI vortices around $x/D = 75$ in Case 1 and $x/D = 55$ in Case 3. A similar effect is observed in the $\mathrm{QR} = 0.57$ simulations where the shear layer reaches the MI around $x/D = 80$ in Case 4 and $x/D = 55$ in Case 5. This also means that the capacity of the shear layer to disturb the MI eddies increases monotonically with the bed discordance.

B. Vortices beneath the free surface

Similar to the simulations conducted by Cheng and Constantinescu [21] for symmetric and asymmetric concordant confluences in very wide channels, SOV cells are generated on both sides of the MI in all five cases. The SOV cells forming on the right and left side of the MI are denoted RSV and LSF, respectively and the index 1 is used to denote the SOV cells situated the closest to the MI. In Case 1 and Case 4, highly coherent bottom attached vortices (BAV) are induced on the left side of the confluence due to the interaction of the neighboring SOV cells with the bottom boundary layer. The BAV vortex rotates in the opposite direction compared to the corotating SOV cells. These vortices are visualized in an instantaneous flow field in Fig. 3 for Case 1 and Case 3. Besides the SOV cells, the Q criterion [50] reveals the presence of a number of streamwise-oriented vortices in the region situated between the bank and the shear layer forming at the same bank. The bank vortices are denoted BV in Fig. 3. These vortices are not SOV cells, as their formation mechanism is different. Such vortices are also observed to form at the inner bank of curved open channels where bank curvature is sufficiently high for a shear layer to form away from the inner wall [51].

Examination of multiple instantaneous flow fields shows that strong interactions take place between the SOV cells situated in the immediate vicinity of the MI and the vertical MI vortices regardless of the bed discordance level. For example, such interactions take place in Case 1 between the MI vortices and the core of RSV1 until $x/D = 60$ and between the MI vortices and the core of RSV2 for $x/D > 80$. Similar interactions are observed on the left side, where LSV1 interacts with the MI vortices. A bottom attached vortex, BAV1, forms in between the cores of LSV1 and LSV2 [Fig. 3(a)]. Once an SOV cell interacts with MI vortices, its core assumes an undulatory/helicoidal shape in the instantaneous flow fields. The downstream part of the core of the SOV cell breaks

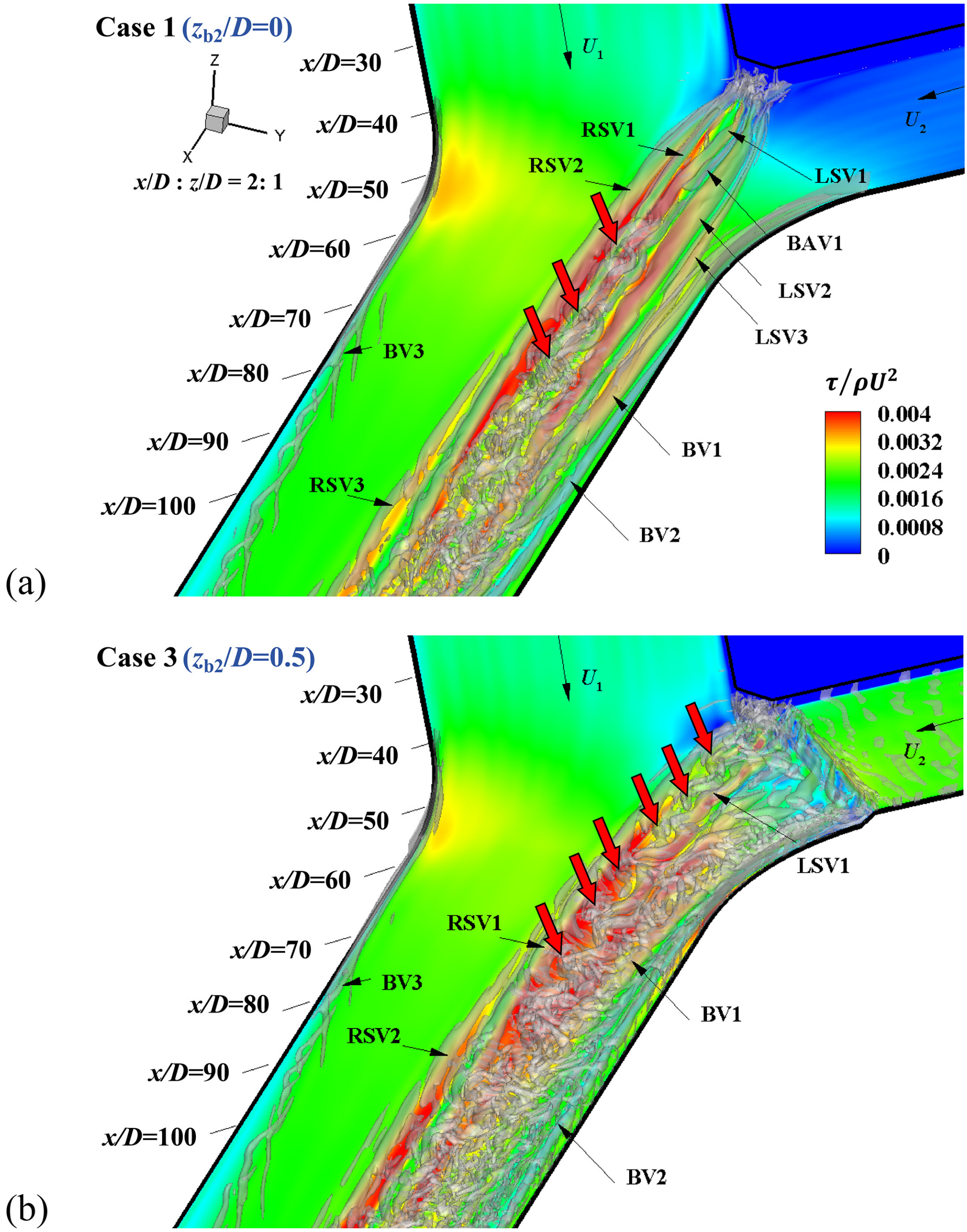

FIG. 3. Coherent structures and bed shear stress distribution in an instantaneous flow field. (a) Case 1; (b) Case 3. A Q isosurface is used to visualize the coherent structures. The red arrows point toward some of the vertical MI vortices.

into multiple elongated eddies, due to the local interactions with the vertical MI vortices. At the same time, the interactions between the SOV cells and the MI vortices lead to severe stretching of the vertical MI vortices. As these vortices lose their coherence, they break into smaller, highly three-dimensional eddies which can be observed in the vorticity fields in Fig. 2 for $x/D > 100$. On

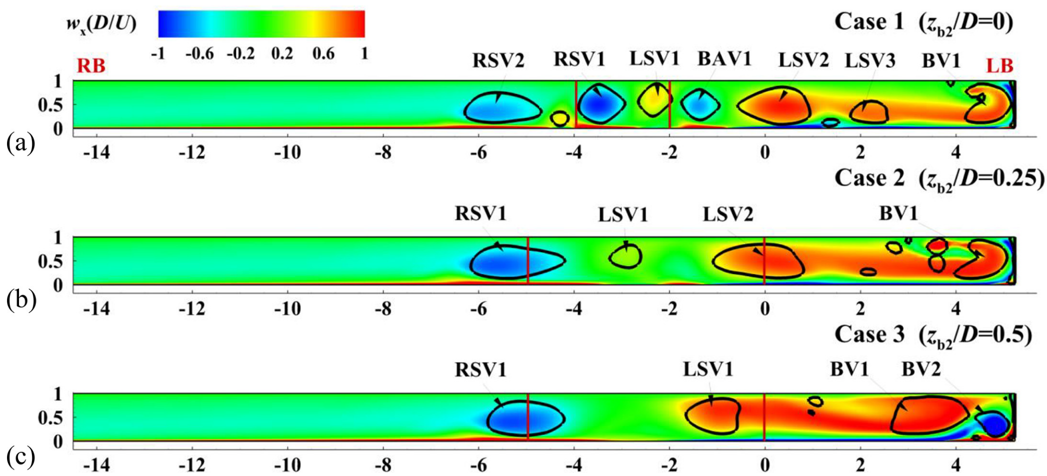

FIG. 4. Streamwise vorticity, $\omega_x D/U$ in the $x/D = 50$ cross section. (a) Case 1; (b) Case 2; (c) Case 3. The vertical lines denote the approximate boundaries of the MI. The cores of the streamwise vortices are visualized using a Q isosurface. LB and RB denote the right bank and left bank, respectively.

the left side of the main confluence channel, interactions also take place between the core of the main bank vortex BV1 and the SOV cells (i.e., LSV2 and LSV3) situated next to it. As observed from Fig. 3, the BV vortices induce a very small amplification of the instantaneous bed shear stress. This is very different from what is observed for the SOV cells. The largest bed shear stresses are induced beneath the cores of these cells.

The presence of a large bed discordance influences the number and the coherence of the SOV cells forming on both sides of the MI. The changes are mostly of a quantitative nature on the right side of the MI with two, rather than three, SOV cells forming on the right side of the MI in Case 3 [Fig. 3(b)] compared to Case 1 [Fig. 3(a)]. The regions of largest shear stress amplification on the right side of the main confluence channel in Case 3 are still situated beneath the cores of RSV1 and RSV2. Major qualitative changes between Case 1 and Case 3 are observed on the left side of the MI. In Case 3, the flow inside the minor tributary separates as it moves over the ramp. This generates lots of smaller eddies in the region where the minor tributary joins the main channel. Moreover, the plunging flow induces large bed shear stresses as it reaches the bed and then accelerates due to the presence of the separated shear layer at the left bank. SOV cells still form on the left side of the MI in Case 3, but the SOV cell, LSV1, extends only up to $x/D = 60$. The much larger and more uniform region of high bed shear stress present on the left side of the main channel in Case 3 is not induced by SOV cells but rather by the core of high velocities originating in the minor tributary.

The streamwise vorticity plots in Fig. 4 visualize the cores of the main streamwise oriented vortices forming inside the main channel. In the concordant bed cases [e.g., see Fig. 4(a) for Case 1], strong SOV cells are generated on both sides of the MI. Consistent with previous investigations (e.g., Refs. [9,10,21]), the cores of the SOV cells are fairly circular and extend until close to the free surface. Strong interactions are observed between the main SOVs on each side of the MI (e.g., between RSV1 and RSV2 and between LSV1 and LSV2). The BAV1 vortex present in between LSV1 and LSV2 sometimes disappears in the instantaneous flow fields as the cores of LSV1 and LSV2 merge. A much smaller bottom-attached vortex is present on the right side of the MI in Case 1 [Fig. 4(a)], but that vortex remains embedded inside the bottom boundary layer.

The main effect of increasing the bed discordance of the minor tributary is to reduce the number of SOV cells on both sides of the MI and to suppress the formation of the BAV vortices (Fig. 4). Meanwhile, the circulation of the main SOV cell forming on the right side of the main channel (i.e., RSV1) increases with increasing bed discordance. On the left side of the confluence, the large region

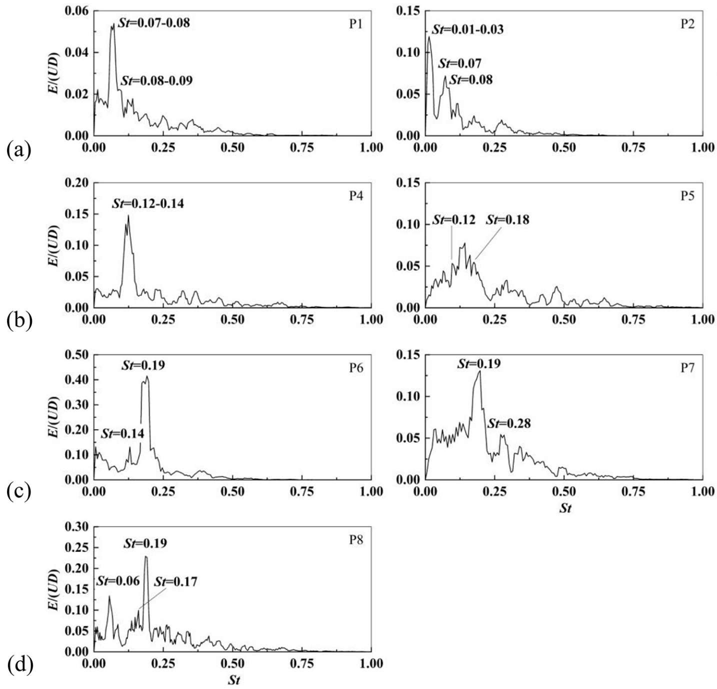

FIG. 5. Nondimensional frequency power spectra of velocity fluctuations at locations situated inside the MI and close to the free surface ($z/D = 0.9$). (a) Case 1; (b) Case 2; (c) Case 3; (d) Case 5. Locations of points is shown in Fig. 2.

containing positive streamwise vorticity penetrating until close to the bank is mostly associated with a secondary flow cell inside which some weaker SOV cells and BAV vortices are present.

C. Frequency power spectra inside the MI

The spectral content of the MI region is analyzed in Fig. 5 that contains frequency power spectra of the spanwise velocity fluctuations near the free surface at different streamwise locations shown in Fig. 2. The horizontal axis shows the Strouhal number, $\mathrm{St} = fD/U$, where f is the frequency. The cut-off frequency for the spectra shown in Fig. 5 corresponds to a Strouhal number between 5 and 10. The instantaneous flow fields at different times (not shown) are used to connect the dynamics of the coherent structures with the energetic frequencies in these power spectra.

For Case 1, where the KH mode dominates, the most energetic frequency at locations situated between 15D from the confluence apex and the region ($60 < x/D < 70$) where the left-bank shear layer starts interacting with the MI eddies corresponds to St = 0.07–0.09 [e.g., see power spectrum for point P1 in Fig. 5(a)]. This range of frequencies corresponds to the dominant passage frequency of the KH vortices. The vortex passage frequency does not decrease with increasing distance from the confluence apex. This means that no merging takes place between neighboring KH vortices, which is different from what was observed by Cheng and Constantinescu [21] at other wide concordant bed confluences and for similar VR values. The absence of vortex pairing over the upstream part of the MI in Case 1 is due to the weak KH mode. Once the KH eddies oriented along the streamwise direction have developed into larger vortices, the KH eddies start interacting with eddies forming over the downstream part of the shear layer originating at the left bank. In Case 1, the MI does not acquire an undulatory shape associated with the start of the transition to the equilibrium regime when pairing of KH vortices is suppressed by bed friction effects. This is an important difference with the simulations of Cheng and Constantinescu [21] performed in very wide channels where the bank shear layers did not reach the MI and the most energetic frequency in the frequency power spectra at locations where vortex pairing was suppressed was associated with the undulatory motions of the MI.

Frequency power spectra for Case 1 at streamwise locations where the KH vortices did not lose their coherence [i.e., $80 < x/D < 100$, see power spectrum at P2 in Fig. 5(a)] still contain a range of energetic frequencies for St = 0.07–0.09. However, a second range of energetic frequencies ($0.01 < \mathrm{St} < 0.03$) is present. These frequencies are associated with the lateral oscillations of the SOV cells that strongly disturb the KH vortices when the core of one of the SOV cells moves toward the MI centerline. Power spectra at locations close to $x/D = 180$ [e.g., see power spectrum at P3 in Fig. 5(a)], where the shear layer originating at the right bank starts interacting with the MI, still show a fairly energetic frequency around St = 0.07 even though the KH vortices are severely stretched and cannot be clearly distinguished from the surrounding 3D energetic eddies [Fig. 2(a)]. The secondary peak near St = 0.025 is associated with the eddies detaching from the right bank shear layer [Fig. 2(a)]. In the other concordant bed simulation (Case 4), the coherence of the MI eddies is very small and the peaks in the velocity power spectra are mostly associated with the lateral oscillations of the SOV cells. For brevity, results are not included.

In Case 2 ($z_{b2} = 0.25\,D$), the KH mode becomes stronger, and a weak wake mode is present inside the MI [Fig. 2(b)]. Power spectra at locations situated in between the end of the stagnation zone and the region ($65 < x/D < 80$) where the left-bank shear layer reaches the MI show a very energetic peak at St = 0.12–0.14 [e.g., see power spectrum at P4 in Fig. 5(b)] associated with the passage of the MI vortices containing positive vertical vorticity. There is no decrease by a factor of two of the dominant frequency, consistent with observations of the instantaneous vorticity fields that show that no vortex pairing takes place between corotating vortices. For $100 < x/D < 130$, the well-defined peak is replaced by a range of energetic frequencies corresponding to $0.12 < \mathrm{St} < 0.18$ [e.g., see power spectrum at point P5 in Fig. 5(b)] as the vertical MI vortices interact with the shear layer eddies and the SOV cells. This is mainly because some of the streaks of positive vorticity from the shear layer merge with corotating MI vortices, while others penetrate in between two corotating MI vortices and are then advected downstream without trying to merge with the MI vortices.

For the highest value of the bed discordance (i.e., $z_{b2} = 0.5\,D$ in Case 3), the wake mode is dominant, and the MI contains more coherent vortices. The passage frequency of these counter-rotating vortices corresponds to St = 0.14. The left bank shear layers sheds very energetic eddies which explains the large peak at St = 0.19 in the power spectrum at point P6 in Fig. 5(c). As fir Case 2, some of the shear layer eddies merge with corotating MI vortices, while others move in between two MI vortices. This explains the presence of a secondary peak around St = 0.28 in the power spectrum at point P7 in Fig. 5(c). No well-defined peaks are observed in the power spectra for $x/D > 120$, which indicates that many of the vertical vortices forming in the upstream part of the MI, or originating inside the left bank shear layer, lost their coherence, consistent with the instantaneous vertical vorticity patterns in Fig. 2(c).

The other simulation (i.e., Case 5) conducted with a bed discordance of $0.5D$ shows that the dominant frequency associated with the passage of vertical vortices inside the upstream part of the MI corresponds to St = 0.17 [e.g., see power spectrum at point P8 in Fig. 5(d)]. So, the increase in QR increases the passage frequency of the wake mode vortices before they start interacting with the left-bank shear layer around $x/D = 60$. As opposed to Case 3, the more coherent wake-mode MI vortices in Case 5 contain negative vorticity rather than positive vorticity. As the shear layer eddies contain positive vorticity, the energy of the MI vortices containing negative vorticity is strongly damped for $x/D > 80$ [see also Fig. 2(e)]. As for Case 3, the shedding frequency of the shear layer eddies is close to St = 0.19, which explains the large peak present in the power spectrum at point P8 in Fig. 5(d). The lower frequencies in the same power spectrum (i.e., $\mathrm{St} \approx 0.06$) are induced by interactions between the MI vortices and the SOV cells. The smaller peak around St = 0.1 corresponds to cases when two corotating vortices containing negative vertical vorticity are slowed down by a large shear-layer eddy penetrating inside the MI followed by merging between these weaker MI vortices. Further downstream (i.e., $100 < x/D < 130$), the frequency power spectra in

Case 5 do not contain any clear dominant frequencies, as the larger-scale eddies lost most of their coherence [Fig. 2(e)].

D. Mixing

The advection of vertical vortices inside the MI is one of the main mixing mechanisms between the fluids originating in the two incoming streams. Mixing takes place primarily by engulfing mostly unmixed fluid from one of the two streams into the MI. The mechanism is essentially the same regardless of which mode dominates inside the MI. The capacity of the vertical vortices to mix fluid scales with the circulation and size of these vortices, as can be seen by comparing the instantaneous distributions of the scalar concentration in a plane, $z/D = 0.9$, close to the free surface in Case 1 [Figs. 2(a) and 6(a)] and Case 3 [Figs. 2(c) and 6(b)]. As discussed in Sec. III A, the formation of strongly coherent counterrotating vortices starting at the back of the stagnation zone in the discordant bed simulation [Fig. 2(c)] is responsible for the strong deformation of the interface in Case 3 [Fig. 6(b)]. By comparison, little mixing occurs near the free surface in Case 1, where a weak KH mode is present, and the circulation of the corotating vortices remains low until $x/D \approx 50$ [Fig. 2(a)]. Moreover, this mixing mechanism weakens significantly in Case 1 as the bed surface is approached [see distribution of C in the $\Delta z/D = 0.15$ plane in Fig. 6(a)] due to the near bed stretching of the lower parts of the cores of the KH vortices. By contrast, the interface deformations near the channel bed in Case 3 [Fig. 6(b)] remain comparable with those observed near the free surface until the MI vortices start being severely stretched by energetic 3D eddies around $x/D = 100$ [Fig. 2(c)]. So, the effect of increasing the bed discordance on mixing driven by the vertical MI vortices is a function on whether, or not, it results in the strengthening of one of the two modes such that high-circulation, larger vortices are generated starting close to the confluence apex.

As for the simulations conducted at angled confluences with a concordant bed by Cheng and Constantinescu [21], the width of the region containing mixed fluid is larger near the bed compared to near the free surface starting some distance from the confluence apex [e.g., see Fig. 6(a) for Case 1]. This is a direct consequence of the formation of strongly coherent SOV cells on both sides of the MI and of the lateral oscillations of their cores. Analysis of the instantaneous flow fields show that when the SOV cell moves inside the MI and part of its core directly interacts with a vertical vortex [Fig. 3(a)], the SOV cell extracts some of the mixed fluid advected inside the core of the MI vortex and then pushes this mixed fluid toward the channel bank. As a result, the MI widens near the channel bed.

The widening of the region containing mixed fluid near the bed is much stronger in the discordant bed cases. The mixing mechanism is different from the one discusses for concordant cases, with the SOV cells on the channel side containing the bed discordance playing a secondary role. In the discordant bed cases, the growth of the region of mixed fluid near the bed is mainly due to the increased flow three dimensionality near the confluence apex that is proportional to the bed discordance height. One should note that this strong widening of the region of mixed fluid near the bed is not dependent on the presence of a sharp transition in the channel bed elevation as in the cases investigated in the present paper the transition in the bed elevation is very gradual. As exemplified in Fig. 6(b) for Case 3, the presence of the bed discordance results in mixed fluid from the stagnation zone being advected out of it into the minor tributary side of the main channel.

As opposed to the concordant bed cases, the mean velocity inside the upstream part of the MI has a strong component oriented toward the bank line on the side of the main channel where the bed discordance is present [see 2D streamlines at $\Delta z/D = 0.15$ in Fig. 6(b)]. This cross-stream velocity component gradually decreases with increasing distance from the channel bed. The thickness of the region where this component is strong scales with the bed discordance height. In particular, its presence explains why mixed fluid is present over about half of the width of the minor tributary channel starting at the confluence apex in Case 3 [Fig. 6(b)]. Once it penetrates on the left side of the main channel, this mixed fluid diffuses vertically as it is advected downstream. The presence of weak SOV cells on the minor tributary side of the main channel contributes to the increase in the

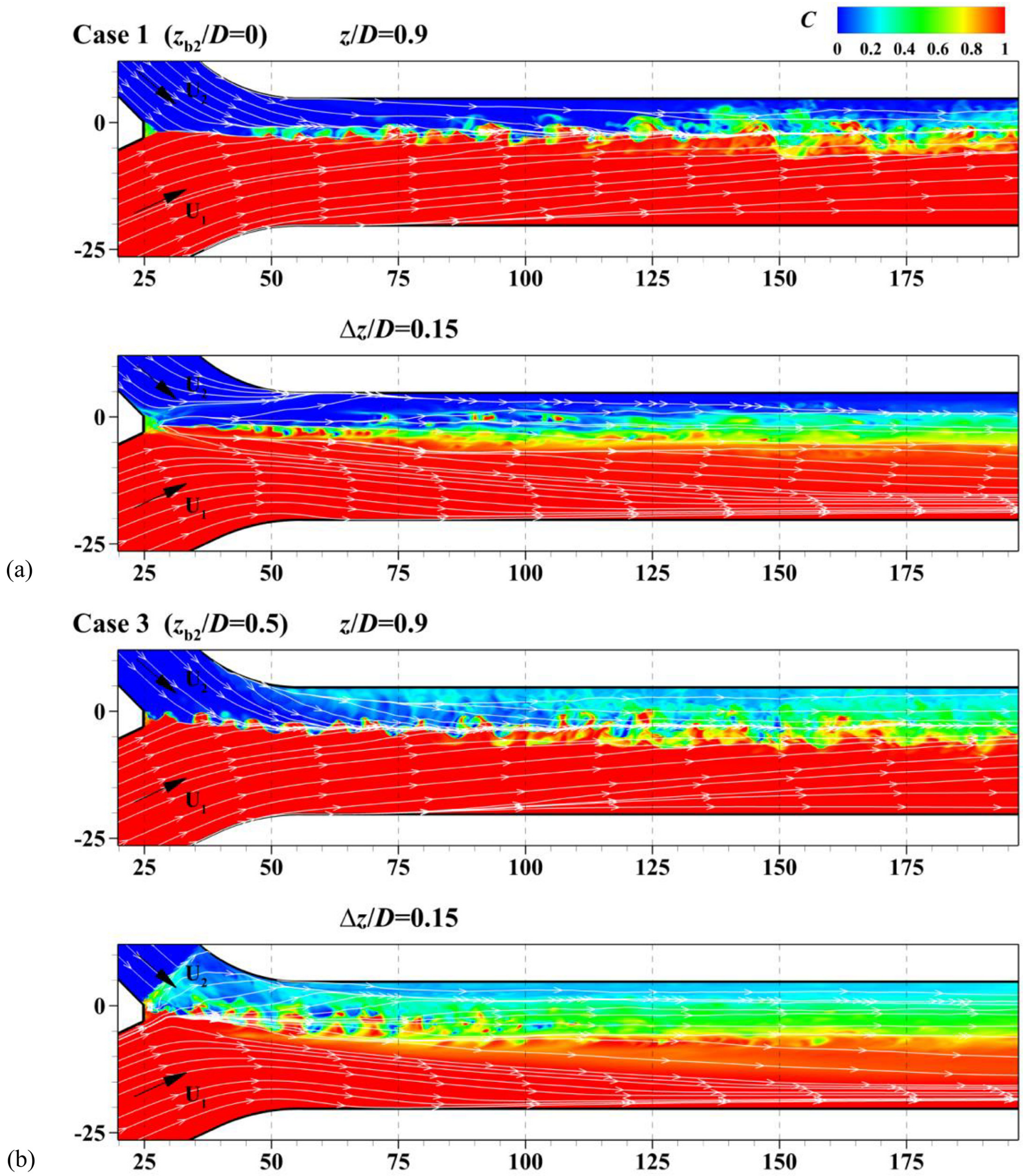

FIG. 6. Nondimensional concentration field, C, in the instantaneous flow near the free surface ($z/D = 0.9$) and near the channel bed ($\Delta z/D = 0.15$). (a) Case 1; (b) Case 3. Also shown are 2D streamline patterns.

lateral width of this region. The strongly mixed fluid observed in Case 3 near the free surface close to the left bank starting at $x/D = 50$ [Fig. 6(b)] is near-bed mixed fluid that is injected into the lower part of the core of BV1 [Fig. 3(b)] and then raises toward the free surface due to the core rotation.

IV. EFFECTS OF THE BED DISCORDANCE ON THE MEAN FLOW STRUCTURE

A. Transverse shift and width of the MI

Figure 7 compares the streamwise variations of the transverse shift of the MI centerline near the free surface, l_{cy}, and of the MI width, δ, with respect to the confluence apex location ($x/D = 25$).

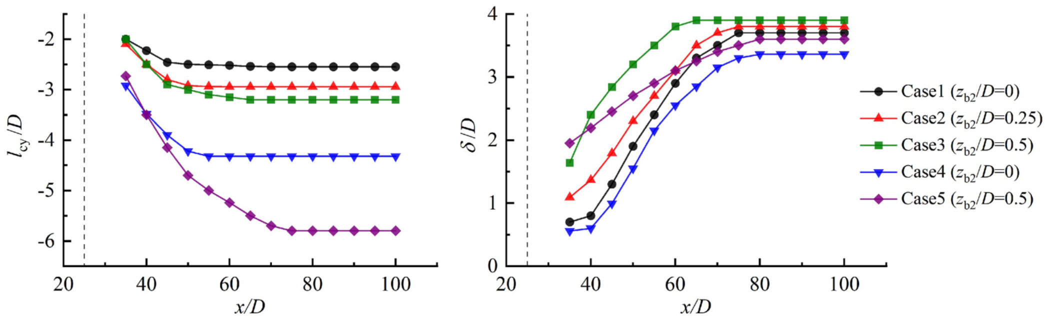

FIG. 7. Shift of the MI centerline, l_{cy}/D (left), and MI width, δ/D (right) near the free surface as a function of the distance from the origin. The vertical dashed line shows the location of the confluence apex.

Given that in most of the simulations the MI vortices become severely stretched and lose most of their coherence around $x/D = 100$, these two variables are only plotted for $25 < x/D < 100$. At a fixed x/D location, the left and right boundaries of the MI correspond to the lateral extent of the region containing MI eddies in the instantaneous flow fields. The centerline is located halfway between the right and left MI boundaries.

In both concordant bed cases, l_{cy} reaches a regime characterized by a small rate of change. The same is true for the MI width that varies little for $x/D > 90$ in Case 1 and Case 4. Though such a regime characterized by a small rate of increase of δ and l_{cy} was also observed over the downstream part of the MI in the concordant bed simulations performed by Cheng and Constantinescu [21], the reasons for the presence of such a regime in the present simulations are very different. In the simulations performed in very wide channels with a MI in the KH mode, vortex pairing was the main mechanism for the growth of δ over the upstream part of the MI. As bed friction effects gradually led to suppression of vortex pairing, the width of the MI reached a regime characterized by a small rate of growth, while the position of its centerline shift varied little with increasing distance from the confluence apex. This behavior was also driven by the gradual decrease of the mean shear across the MI with increasing x/D.

By contrast, even in the concordant bed simulation (Case 1) where the MI is in the KH mode [Fig. 2(a)], vortex pairing is not observed. The initial growth of the MI width is driven by the change in the orientation of the KH eddies and by the fact that these eddies become more circular as they are advected downstream. In Case 4 [Fig. 2(d)], the MI remains very thin until it breaks due to strong interactions with the SOV cells ($x/D \approx 65$) and with the eddies detaching from the left-bank shear layer ($x/D \approx 85$). In both concordant bed simulations, the regime characterized by a small rate of change of l_{cy} begins immediately downstream of the location where the shear layer eddies start interacting with the MI vortices [i.e., $x/D = 65$ for Case 1 and $x/D = 85$ for Case 4, see also Figs. 2(a) and 2(d)]. The MI width continues to grow for some distance because of the interactions and merging between the shear layer eddies and some of the MI vortices before reaching a regime characterized by a small rate of growth. So, for angled asymmetric confluences with common values of the aspect ratio of the confluence channels, the spatial development of the MI is significantly affected by its interaction with the shear layers forming at the banks once they penetrate inside the MI. There is no evidence of a transition to an equilibrium regime in such cases.

For both values of the discharge ratio, the effects of increasing the bed discordance on δ and l_{cy} are qualitatively similar. The centerline of the MI switches toward the right bank near the free surface (Fig. 2) primarily because of the higher free-surface velocities inside the minor tributary channel upstream of the start of the change in the bed elevation. That core of higher velocities pushes the MI toward the right, which increases l_{cy}. As for the concordant bed cases, the MI in the discordant bed cases reaches a regime characterized by a close to constant value of l_{cy} [Fig. 7(a)]. In the QR = 0.36 simulations, the far field value of l_{cy} decreases from $-2.5D$ in Case 1 to about $-3.0D$

in Case 2 and to $-3.3D$ in Case 3. The increase of the relative discharge of the minor tributary pushes the MI toward the right, which explains the larger values of $|l_{cy}|$ in Case 4 compared to Case 1. The far field value of l_{cy} in the QR = 0.57 simulations decreases from $-4.4D$ in Case 4 ($z_{b2} = 0\,D$) to $-5.8D$ in Case 5 ($z_{b2} = 0.5\,D$).

As already discussed, the increase in bed discordance triggers the transition to a dominant wake mode from of a weak KH mode. This explains why the MI width close to the confluence apex is much larger in the discordant bed cases where strong counterrotating vortices are forming at the back of the stagnation zone compared to the corresponding concordant bed cases [see Figs. 2 and 7(b)]. Meanwhile, the rates of growth of δ are higher in between the apex and the region where the left-bank shear layer reaches the MI, as the cores of the KH vortices become more circular. If the wake mode dominates, the lateral movement of the counterrotating MI vortices is comparatively lower, as the cores of these vortices diffuse little until they start interacting with the left-bank shear layer. Past of the region where the MI interacts with this shear layer, the MI width becomes close to constant, and its value increases monotonically with increasing bed discordance height for constant QR [Fig. 7(b)].

B. Streamwise-oriented coherent structures

Figure 8 visualizes the SOV cells and the other streamwise-oriented vortices in the mean flow fields for the QR = 0.36 simulations. As opposed to the instantaneous flow fields (Fig. 3), the cores of the SOV cells are fairly straight in the mean flow. This also allows us to get a clearer picture of the main cells forming inside the main channel, their positions relative to the MI and their lengths. Additionally, Fig. 9 compares the variation of the circulation along the cores of the main SOV cells forming on the two sides of the MI in the five simulations. The circulation is defined as the integral of the streamwise vorticity, ω_x, inside the core of the SOV cell. A threshold value of $0.2U/D$ was used to define the core of the SOV cell.

Three corotating SOV cells form on both sides of the MI with an additional counterrotating cell, BAV1, on the left side of the MI in Case 1 [Fig. 8(a)] and Case 4. Starting at about $60D$ from the confluence apex, RSV2 is the main SOV cell on the right side of the MI in Case 1. Its core extends up to $x/D = 140$ in Case 1 and $x/D = 130$ in Case 4 [Fig. 9(a)]. The circulation of RSV2 is comparable in the two concordant bed simulations [Fig. 9(a)]. A third SOV cell, RSV3, is present inside the main channel for $x/D > 70$. The coherence of this cell is relatively low in Case 1, and this cell does not move close to the MI. On the left side of the MI, LSV1 extends only up to $x/D \approx 60$, downstream of which the more coherent cell LSV2 is situated in the vicinity of the MI. The main effect of increasing QR from 0.36 (Case 1) to 0.57 (Case 4) is to decrease the circulation of RSV2 by about 25% and to increase the circulation of LSV2 by more than 100% [Fig. 9(a)].

The increase of the bed discordance height to $0.25D$ reduces the number of SOV cells forming on the left side of the MI from three in Case 1 to two in Case 2 [Fig. 8(b)]. The circulation of LSV2 is by about 50% larger in Case 2 compared to Case 1 [Figs. 8(a), 8(b), 9(a), and 9(b)]. On the right side, the coherence of RSV1 increases in Case 2, while that of RSV2 decreases [Figs. 9(a) and 9(b)]. Moreover, RSV2 forms around $x/D = 60$ in Case 2 rather than close to the confluence apex. The increase of the bed discordance height from $0.25D$ (Case 2) to $0.5D$ (Case 3) results in a large increase of the coherence of LSV1 near the confluence apex, in a slight decrease of the coherence of RSV1 and RSV2, and in the suppression of one SOV cell (i.e., LSV2) on the left side of the MI [Figs. 8(b), 8(c), 9(b), and 9(c)]. Interestingly, the increase of QR from 0.36 to 0.57 has only a mild effect on the coherence of the main SOV cells in the simulations conducted with a bed discordance height of $0.5D$ [Fig. 9(c)].

As for other concordant, high angle confluences (e.g., Refs. [9,10,7,21]), some of the SOV cells forming in the present simulations are subject to bimodal oscillations, which enhances their capacity to induce mixing and sediment entrainment. The distribution of the mean pressure fluctuations in the $x/D = 30$ cross section in Case 1 [Fig. 10(a)] shows the presence of two peaks inside the cores of LSV1 and RSV1, which means that the lateral oscillations of these SOV cells are

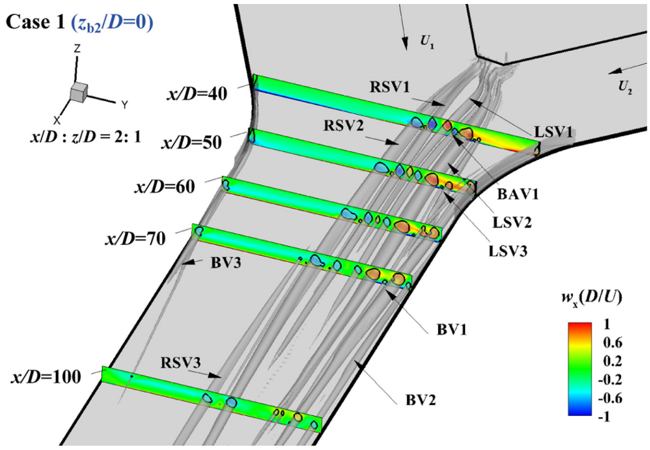

(a)

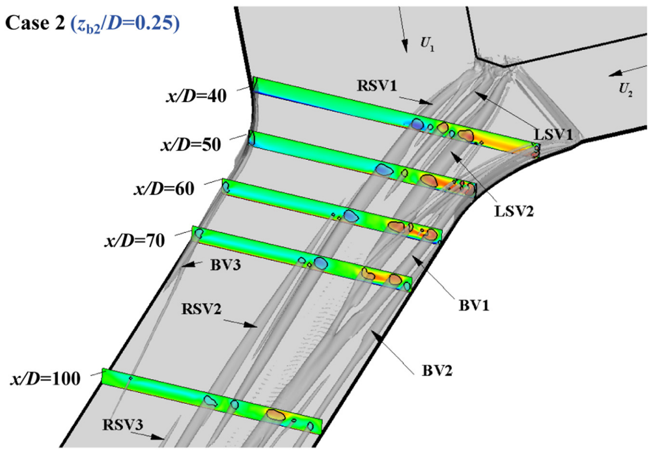

(b)

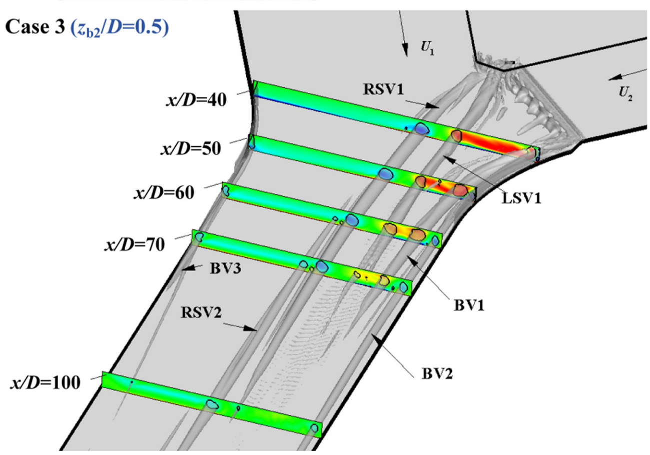

(c)

FIG. 8. Coherent structures in the mean flow. (a) Case 1; (b) Case 2; (c) Case 3. A Q isosurface is used to visualize the coherent structures. Also shown are the distributions of the nondimensional streamwise vorticity in several cross sections (x/D = 40, 50, 60, 70, and 100).

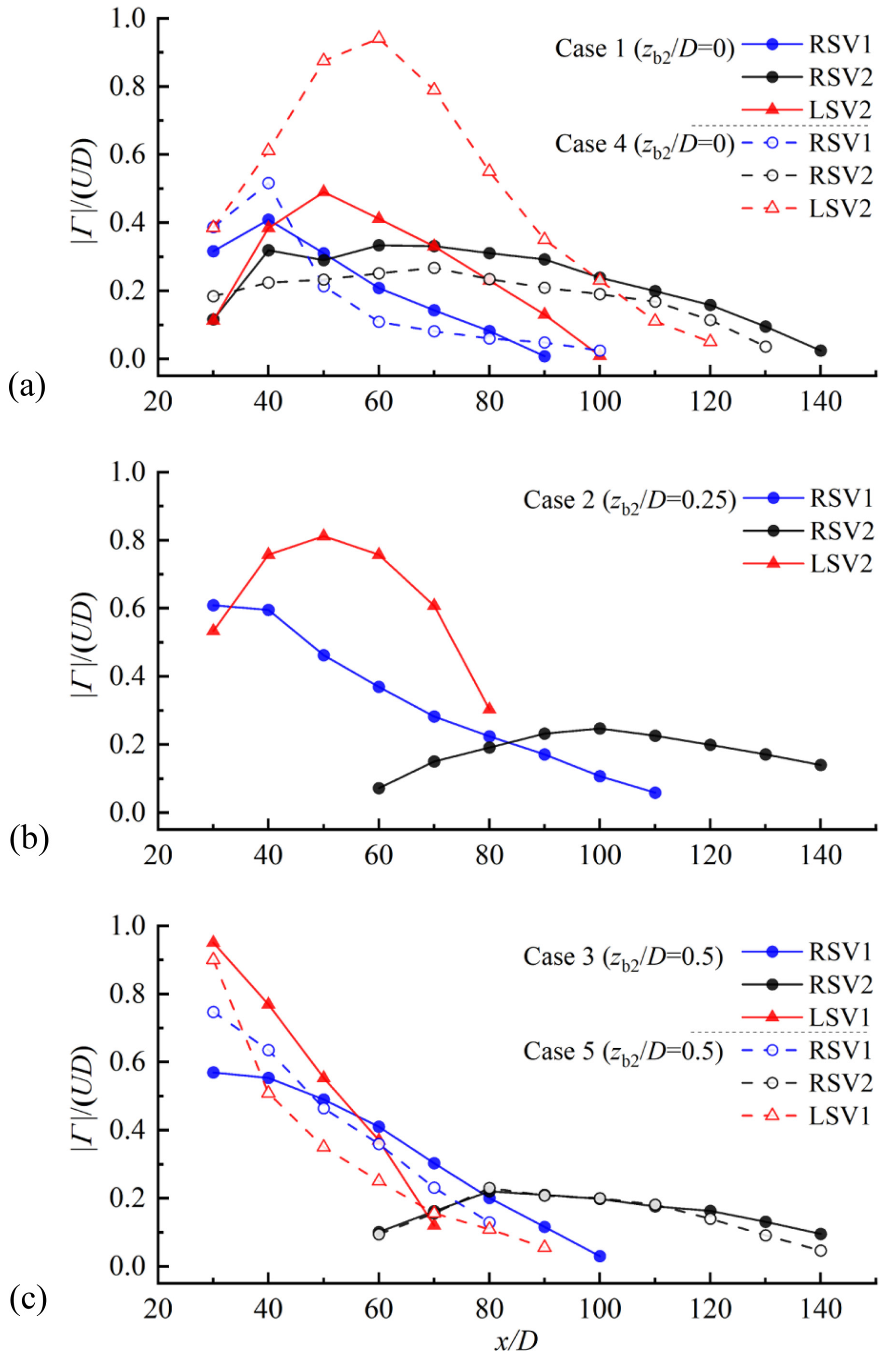

FIG. 9. Streamwise variation of the nondimensional circulation magnitude of the main SOV cells. (a) Case 1 and Case 4; (b) Case 2; (c) Case 3 and Case 5.

bimodal [9]. As the bed discordance height increases to $0.25D$, the bimodal oscillations of RSV1 are suppressed. However, the core of LSV1 is still subject to strong bimodal oscillations in the $x/D = 30$ cross section [Fig. 10(b)]. As the bed discordance height is further increased to $0.5D$, the bimodal oscillations of LSV1 are totally suppressed [Fig. 10(c)]. The high mean pressure

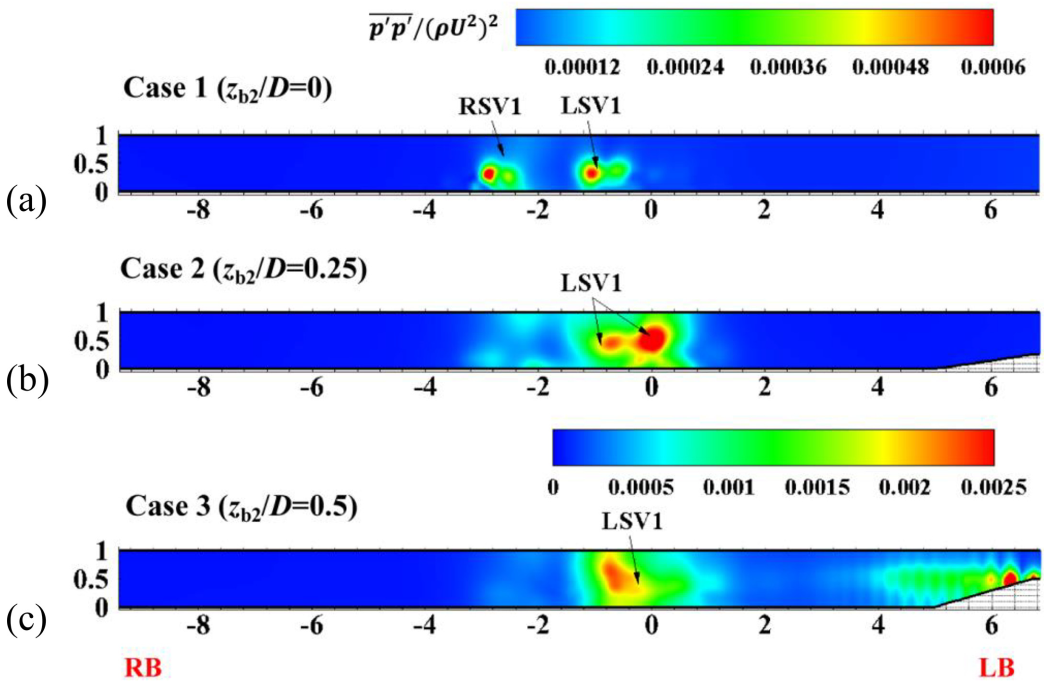

FIG. 10. Mean pressure fluctuations, $\overline{p'p'}/(\rho U^2)^2$ in the $x/D = 30$ cross section. (a) Case 1; (b) Case 2; (c) Case 3. LB and RB denote the right bank and left bank, respectively.

fluctuations observed in Fig. 10(c) near the region where the bed elevation changes are due to the separated shear layer and recirculation bubble induced by the flow separating over the ramp in Case 3.

The variation of the bed discordance height also affects the position and coherence of the vortices forming close to the left bank. As z_{b2} changes from 0D in Case 1 to 0.25D in Case 2, the circulation of BV1 increases and its core moves further away from the left bank, such that it starts merging with LSV2 [Figs. 8(a) and 8(b)]. Increasing the bed discordance height to 0.5D decreases the length of BV1 which penetrates only up to $x/D = 80$ in Case 3 [Fig. 8(c)] compared to $x/D \approx 125$ in Case 2 [Fig. 8(b)].

C. Mean streamwise velocity

Besides the angles between the tributary channels and the downstream channels, the redistribution of the streamwise momentum downstream of the confluence apex is strongly affected by the presence of streamwise-oriented vortices (e.g., SOV cells, BV vortices) and the generation of shear layers at the banks of the main channel (see Figs. 2 and 8). As shown by the mean streamwise velocity plots in the $z/D = 0.9$ plane in Fig. 11, the flow near the free surface accelerates in the streamwise direction downstream of the confluence apex ($x/D = 25$) regardless of the bed discordance level. This is due mainly to the rotation of the core of high velocity inside each tributary as they enter the main channel. Meanwhile, regions of low streamwise velocity are present near the free surface in the vicinity of the main shear layers originating at the left and right banks (Fig. 2). Near the free surface, the size of the stagnation zone is not affected by the level of bed discordance as the boundary layers remain attached to the lateral converging walls until the confluence apex (see streamlines in Fig. 11). The main effect of increasing the bed discordance is to reduce the streamwise momentum amplification near the entrance into the main channel on the minor tributary side.

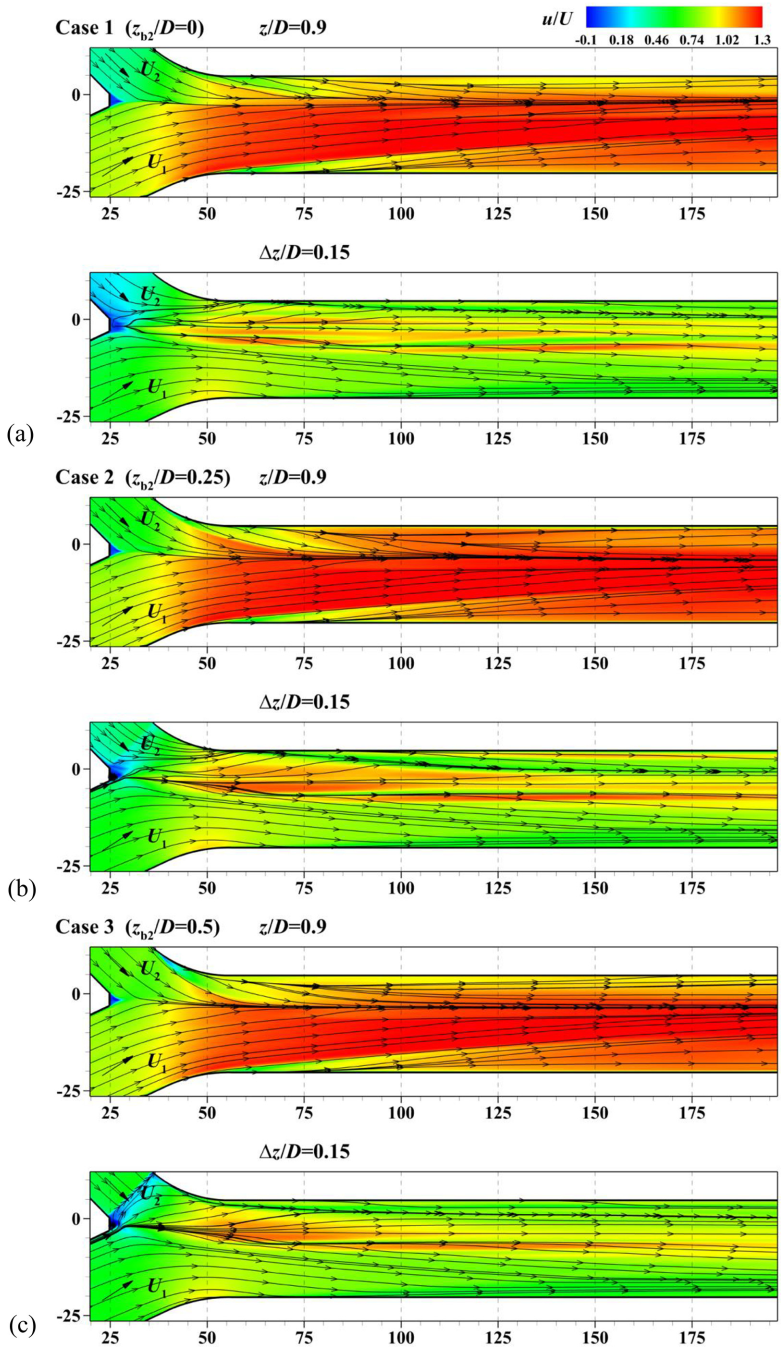

FIG. 11. Nondimensional streamwise velocity, u/U, and 2D streamline patterns in the mean flow near the free surface ($z/D = 0.9$) and near the channel bed ($\Delta z/D = 0.15$). (a) Case 1; (b) Case 2; (c) Case 3.

Over the deeper parts of the channels, the redistribution of the streamwise momentum is mainly controlled by the most coherent SOV cells, at least for cases with a concordant bed [e.g., see Fig. 11(a)] and with a moderate level of bed discordance [Fig. 11(b)]. Regions of high streamwise velocity are induced on one of the sides of the core of each SOV cell where free surface, higher-speed fluid is advected toward the bed by the rotational flow inside the core of each cell. This induces the elongated regions of high streamwise velocity magnitude in the $\Delta z/D = 0.15$ frames in Fig. 11. This phenomenon is present even for cases with a high level of bed discordance (i.e., $z_{b2} = 0.5\,D$) on the main tributary side of the main channel. By contrast, the main region of high streamwise velocity on the minor tributary side is induced by the core of high velocity from the minor tributary that reaches the channel bed downstream of the separation bubble forming over the ramp (see discussion of Fig. 16 in Sec. VI).

V. TURBULENCE STATISTICS

The TKE is calculated as half of the sum of the normal Reynolds stresses in the three directions. A strong nonuniformity of the TKE distribution in the vertical direction is observed in all simulations. This is mainly caused by the decrease in the coherence of the MI vortices due to bed friction and the sudden reduction of the advective velocity close to the channel bed. The other main reason for the vertical nonuniformity of the TKE is the presence of SOV cells and other streamwise oriented vortices.

In Case 1 [Fig. 12(a)], the largest TKE values near the free surface are observed inside the thin region where KH vortices are forming close to the centerline of the MI. A second thin region of high TKE is present between $x/D = 75$ and $x/D = 90$. This region is induced by the energetic eddies separating from the left-bank shear layer [Fig. 2(a)]. The TKE is also amplified inside the region where highly unsteady SOV cells are present. The RSV2 and RSV3 cells are subject only to minor oscillations in the lateral direction. Near the channel bed, the passage of the KH vortices has a relatively minor effect on the TKE and the largest amplification of the TKE in between the confluence apex and $x/D = 45$ is induced by the lateral oscillations of LSV1. At larger distances from the confluence apex, the TKE distributions near the bed and the free surface are qualitatively similar. The streaks of high TKE present in Case 1 on the left side of the MI for $x/D > 65$ are induced by the unsteadiness of the bank vortices BV1 and BV3.

The TKE distributions are qualitatively similar in the Case 3 [Fig. 12(b)] and Case 5 [Fig. 12(c)] simulations for which the bed discordance height is $0.5D$. Near the free surface, the main change with respect to the concordant bed cases is the large amplification of the TKE inside the MI in between the confluence apex and $x/D = 90$, where counterrotating MI vortices are advected [Figs. 2(c) and 2(e)]. The thickness of this region increases with increasing QR. The peak TKE levels inside this region are more than three times larger compared to the ones induced inside the MI in Case 1. The other region of high TKE near the free surface in Case 3 and Case 5 corresponds to the left-bank shear layer that generates highly energetic eddies. Bed friction and vortex stretching reduce the coherence of the MI vortices as they move away from their formation region. For $x/D > 60$, the width of the region of relatively high TKE is between 2D and 3D larger near the bed compared to near the free surface. The main reason is the presence of the high-circulation vortex RSV2 [Fig. 8(c)]. This quasisteady SOV cell advects near-bed fluid situated beneath its core toward the right bank. This fluid contains highly 3D, energetic eddies.

The distributions of the time- and depth-averaged primary shear stress, $\langle u'v' \rangle$, in Cases 1, 2, and 3 (see Fig. 13) also show that turbulence is strongly amplified by the vertical vortices shed over the upstream part of the MI ($25 < x/D <$ 60–75) and by the streamwise oriented vortices (SOV cells and bank vortices that are subject to lateral oscillations) forming primarily on the minor tributary side of the confluence. Another area of strong amplification of the primary shear stress is in the region (60–7 $< x/D <$ 110–125) where the MI vortices interact with the eddies shed from the downstream part of the shear layer forming at the left bank [Figs. 2(a)–2(c)]. The main effects of increasing the bed discordance level are the increase magnitude of $\langle u'v' \rangle$ inside the wake region, as the wake mode becomes dominant [see also Figs. 2(a)–2(c)] and inside the shear layer forming at the left bank that contains vortices in Case 3 [Fig. 2(c)].

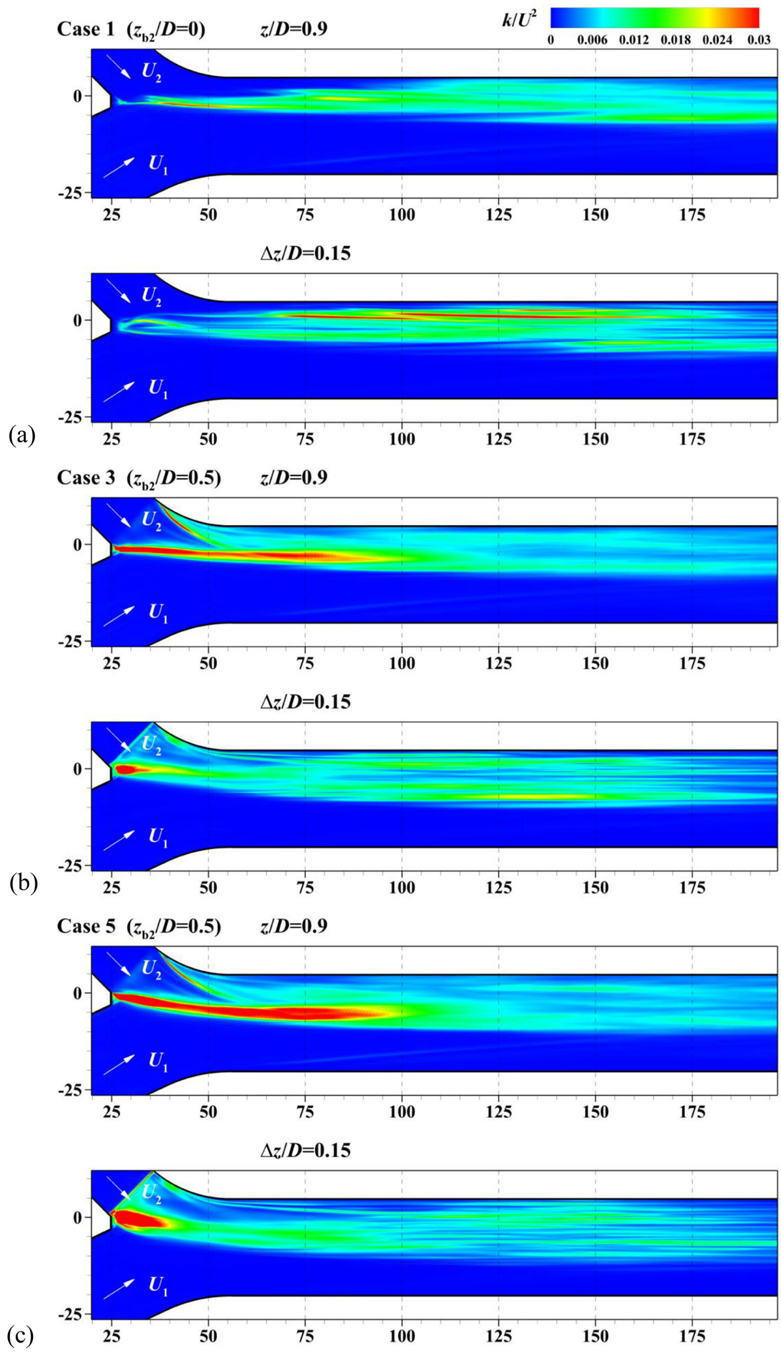

FIG. 12. Turbulent kinetic energy, k/U^2, near the free surface ($z/D = 0.9$) and near the bed ($\Delta z/D = 0.15$). (a) Case 1; (b) Case 3; (c) Case 5.

VI. MIXING IN THE MEAN FLOW

Mixing between the fluids in the two tributaries is numerically investigated by analyzing the mean scalar concentration fields. In all simulations, the size of the region containing mixed fluid

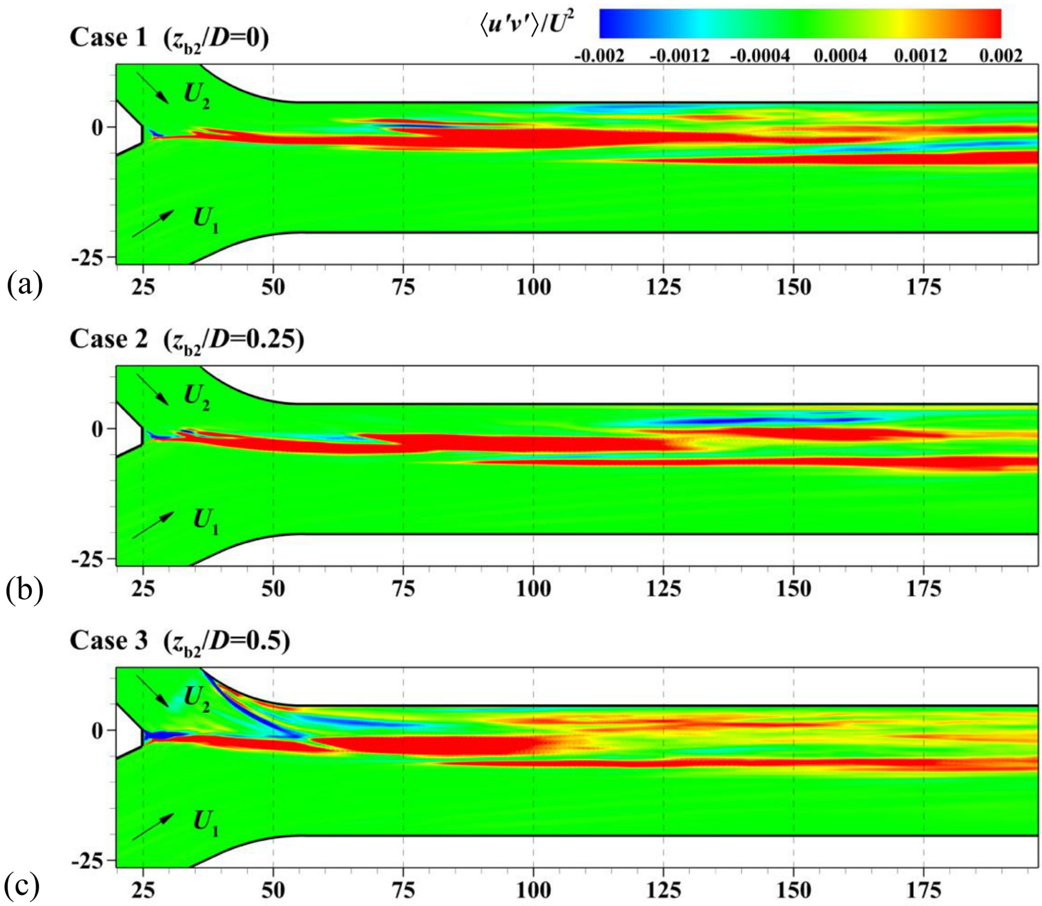

FIG. 13. Time- and depth-averaged primary shear stress, $\langle u'v' \rangle/U^2$. (a) Case 1; (b) Case 2; (c) Case 3.

(e.g., fluid with a nondimensional scalar concentration $0.1 < C < 0.9$) is larger near the bed compared to near the free surface (e.g., see Fig. 14). The main reason is the presence of SOV cells on both sides of the MI (Fig. 8). The (primary) SOV cells situated closest to the MI extract mixed fluid inside their cores as they penetrate inside the MI during their lateral oscillations. Moreover, due to swirl inside the SOV cell, some of the MI fluid situated in the bed vicinity is advected beneath the core of that SOV cell toward the bank line. If secondary, corotating SOV cells are present, this near-bed mixed fluid is pushed farther toward the bank line by the secondary cells. As the SOV cells eventually break into smaller scale turbulence (Fig. 3), the scalar advected inside their cores is released to the surrounding fluid.

In Case 1, where a weak KH mode is present inside the MI, the mixing between the fluids originating in the two incoming streams is negligible in between the end of the stagnation zone and $x/D = 40$–45. This is expected, given that the elongated KH eddies remain closely aligned with the streamwise direction in this region. The cells LSV1 and RSV1, though strongly coherent starting at the confluence apex, cannot extract mixed fluid from the MI until $x/D \approx 40$. For example, the distribution of C at $x/D = 30$ [Fig. 15(a)] shows only a very thin layer of mixed fluid leaving the MI near the bed because of RSV1. Despite being subject to bimodal oscillations [Fig. 10(a)], the cores of LSV1 and RSV1 are too far from the MI to have a major effect on mixing close to the confluence apex. This changes around $x/D = 40$ where LSV1 gets close to the MI and generates a lateral intrusion of mixed fluid beneath its core [Fig. 15(a)]. The formation of the intrusion also

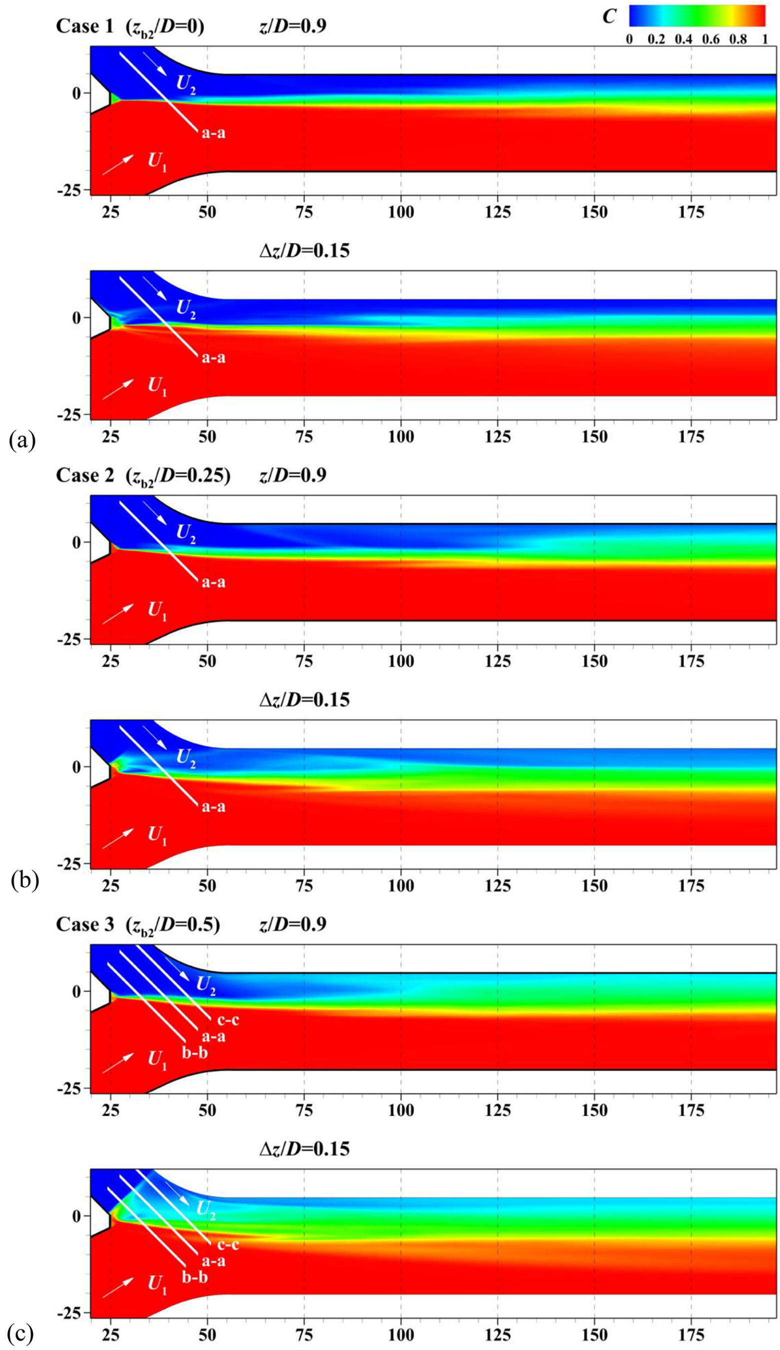

FIG. 14. Nondimensional concentration field, C, and 2D streamline patterns in the mean flow near the free surface ($z/D = 0.9$) and near the channel bed ($\Delta z/D = 0.15$). (a) Case 1; (b) Case 2; (c) Case 3.

explains the sudden increase in the width of region containing mixed fluid near the bed, while no noticeable change occurs near the free surface around $x/D = 40$ [Fig. 14(a)]. The sudden increase of the width of the region of mixed fluid near the free surface for $x/D > 45$ is primarily due to

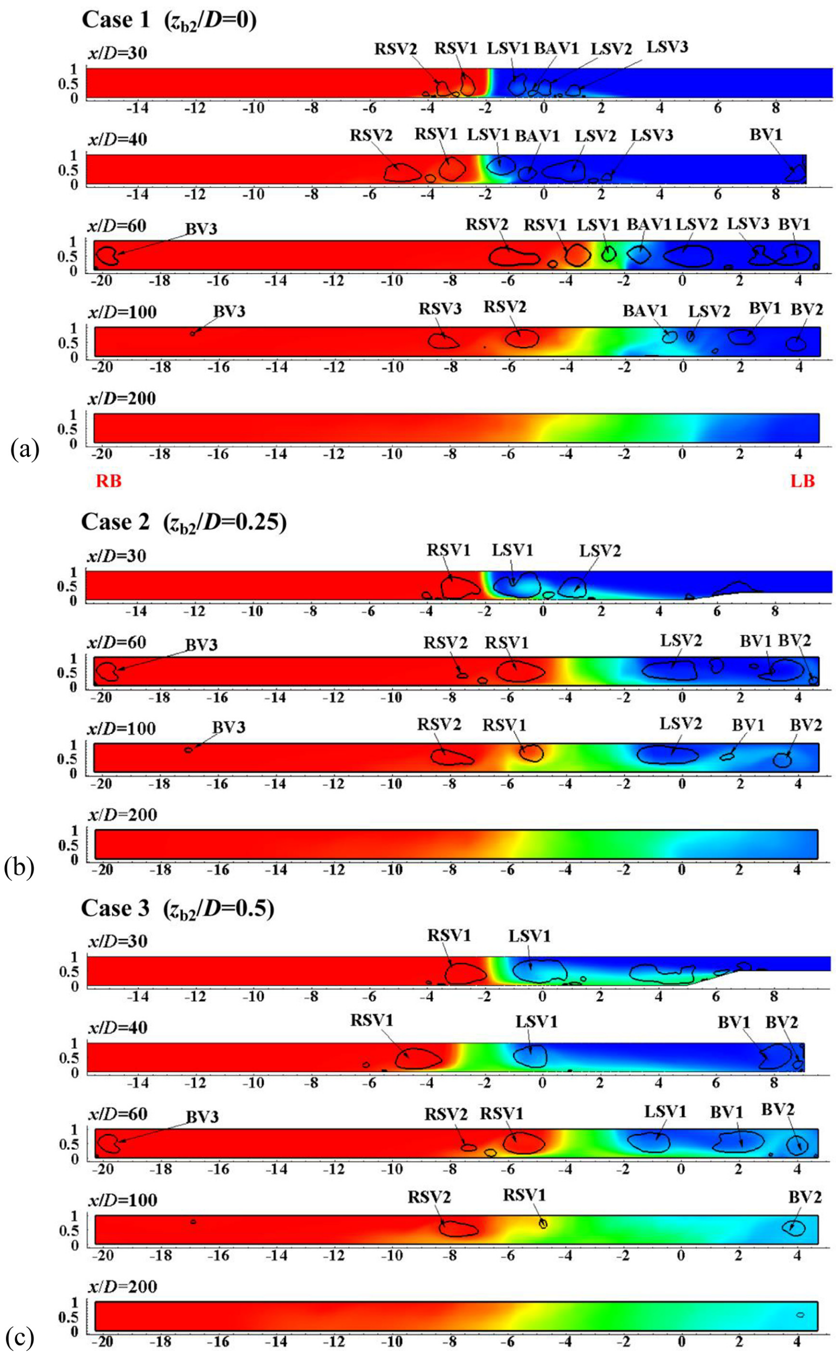

FIG. 15. Nondimensional concentration, *C*, and 2D streamline patterns in the mean flow in several cross sections. (a) Case 1; (b) Case 2; (c) Case 3. The legend is the same as in Fig. 14. Also shown are the cores of the main SOV cells. LB and RB denote the right bank and left bank, respectively.

LSV1 moving inside the MI and to BAV1 moving near the edge of the MI. These counterrotating vortices advect fluid near the free surface and from there toward the left bank [see distribution of C at $x/D = 60$ in Fig. 15(a)]. On the right side of the MI, RSV1 extracts some limited amount of MI fluid close to the bed. The other mechanism for the growth of the region containing mixed fluid is the rotation of the KH eddies and their increase in size between $x/D = 55$ and $x/D = 75$ [Fig. 2(a)]. The width of the region of mixed fluid remains close to constant near the free surface as the KH vortices cease their growth and LSV1 and BAV1 start losing their coherence. The elongated longitudinal region of mixed fluid present on the left side of the channel starting around $x/D = 85$ [see $z/D = 0.15$ section in Fig. 14(a)] is induced by LSV2. Moreover, RSV2 gets sufficiently close to the MI to increase the lateral penetration of mixed fluid leaving the MI near the bed [e.g., see $x/D = 100$ section in Fig. 15(a)]. Once the SOV cells disappear (i.e., for $x/D > 130$), the width of the region of mixed fluid remains close to constant near the bed [Fig. 14(a)]. This is accompanied by a gradual increase in the level of uniformity of C in the vertical direction [e.g., see $x/D = 200$ section in Fig. 15(a)]. The presence of 3D energetic eddies in between the MI and the left bank for $x/D > 100$ [Fig. 2(a)] enhances local mixing and contributes to the vertical profile of C becoming more uniform for $x/D > 150$.

In Case 2, the KH mode is stronger and highly coherent KH vortices start forming at a smaller distance from the confluence apex, which explains the larger width of the region of mixed fluid near the free surface [Fig. 14(b)] compared to Case 1 [Fig. 14(a)] until $x/D = 40$. At larger distances, LSV1 starts interacting with the MI. The effect of LSV1 on mixing is even stronger near the bed where it extracts mixed fluid from the MI. This SOV cell disappears by $x/D = 60$ [Fig. 8(b)]. However, LSV2 moves close to the MI and plays a similar role to that of LSV1 at upstream locations, as illustrated by the distribution of C in the $x/D = 60$ section in Fig. 15(b). Interestingly, LSV2 does not entrain mixed fluid inside its core. Rather, LSV2 advects mixed fluid toward the left bank beneath its core and from there toward the free surface [see $x/D = 100$ section in Fig. 15(b)]. By this location, the growth of the region of mixed fluid close to the bed is not entirely driven by LSV1, as RSV1 also generates a near-bed lateral intrusion of mixed fluid. As a result, the width of the region of mixed fluid in Case 2 is close to two times larger near the bed compared to near the free surface in between $x/D = 80$ and $x/D = 120$. As some of the mixed fluid advected beneath LSV2 reaches the free surface, the width of the region containing mixed fluid close to the free surface increases suddenly around $x/D = 120$. As for Case 1, once the SOV cells on the left side of the main channel disappear around $x/D = 150$, the interface between the unmixed fluid from the main tributary and the region containing mixed fluid becomes closer to vertical [see $x/D = 200$ section in Fig. 15(b)]. The mixing remains nonuniform on the minor tributary side [see $x/D = 200$ section in Fig. 15(b)].

While the effects of the main SOV cells on mixing are qualitatively similar in Case 2 [Fig. 15(b)] and Case 3 [Fig. 15(c)], the increase in the size of the mixing region near the bed and near the free surface in Case 3 is driven by the near-bed intrusion of mixed fluid on the minor tributary side [Figs. 14(b), (14c), and 16] and, to a smaller extent, by the higher-circulation vortices populating the upstream part of the MI [Fig. 2(c)]. In particular, the near-bed region between the MI and the ramp is fully occupied by mixed fluid in the $x/D = 30$ section [Fig. 15(c)]. By $x/D = 40$, the intrusion of near-bed mixed fluid penetrated until about 2D from the left bank. By contrast, near the free surface, the width of the region containing mixed fluid is comparable to the MI width until $x/D = 60$ [Fig. 14(c)], as mixing is driven by the vertical MI vortices [Fig. 2(c)]. As LSV1 gets close to the MI, it increases the extraction of mixed fluid from the MI into the near-bed intrusion [e.g., see $x/D = 60$ section in Fig. 15(c)]. Then, the counterrotating bank vortices BV1 and BV2 raise the front of the near-bed intrusion of mixed fluid toward the free surface. This explains the formation of a free-surface region of mixed fluid at the left bank in between $x/D = 50$ and $x/D = 95$ that is separated from the main region of mixed fluid [see $z/D = 0.9$ section in Fig. 14(c)]. A near-bed intrusion of mixed fluid is also generated on the major tributary side of the main channel first by RSV1 (see $x/D = 60$ section in Fig. 15c) and then by RSV2 [see $x/D = 100$ section in Fig. 15(c)]. By $x/D = 200$, most of the fluid in between the right boundary of the MI and the left bank is well

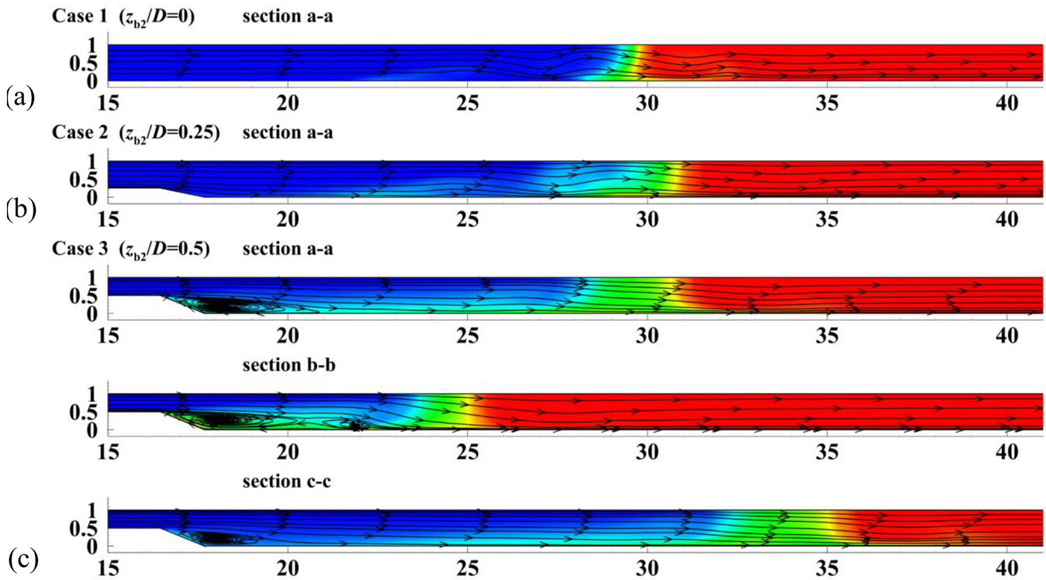

FIG. 16. Nondimensional concentration field, C, and 2D streamline patterns in the mean flow. (a) Case 1, section a-a; (b) Case 2, section a-a; (c) Case 3, sections a-a, b-b, and c-c. The legend is the same as in Fig. 12. The positions of the sections are shown in Fig. 14.

mixed in Case 3. The mixing mechanisms in Case 5 are qualitatively similar to those observed in Case 3.

Comparison of the mixing patterns in Fig. 14 for the QR $= 0.36$ simulations shows that mixing increases with increasing bed discordance. The effect is especially strong near the bed where the size of the region of mixed fluid increases substantially even for a moderate level of bed discordance [Figs. 14(a) and (14b)]. This effect is driven by the increase in the level of three dimensionality of the flow that results in some of the near-bed fluid situated close to the confluence apex being advected from the MI toward the left bank [see 2D streamline patterns in Figs. 6(b) and 11(c)]. The distribution of C in section a-a shows a near bed intrusion of mixed fluid extending from the end of the ramp to the MI in Case 3 [Fig. 16(c)]. Such an intrusion is absent in the concordant bed case [Fig. 16(a)]. As the level of bed discordance increases, near-bed mixed fluid from the MI penetrates over a larger distance toward the left bank [e.g., compare C distributions in section a-a in Figs. 16(b) and 16(c)], close to the end of the ramp. For example, close to the bed surface, the intrusion width is about $b_2/3$ in Case 2 [Figs. 14(b) and 17(b)] and $3b_2/4$ in Case 3 [Figs. 14(c) and 17(c)]. The main reason for the formation of this intrusion of MI fluid is the presence of the separation bubble for sufficiently high bed discordance (Fig. 16). MI fluid is advected inside the core of this recirculation bubble and from there into the minor tributary side of the main channel. This phenomenon is illustrated in Figs. 17(b) and 17(c) where 3D stream traces launched close to the right lateral wall of the confluence apex move around the stagnation zone into the recirculation bubble induced by the ramp before moving downstream inside the minor tributary side of the main channel. By contrast, stream traces launched on either side of the confluence apex remain on the same side of the MI in the concordant bed cases [e.g., see Fig. 17(a)]. The amount of MI fluid advected on the minor tributary side also growth monotonically with z_{b2}/D. Downstream of the ramp, some of this mixed fluid starts being entrained into the SOV cells above it [e.g., see $x/D = 30$ section for Case 2 in Figs. 15(b) and for Case 3 in Fig. 15(c)].

Besides the mean flow coherent structures and 3D flow features near the confluence apex, turbulence also plays a significant role in mixing the two streams. Given that downstream of the confluence apex, the mean flow direction is aligned with the streamwise direction, the primary scalar

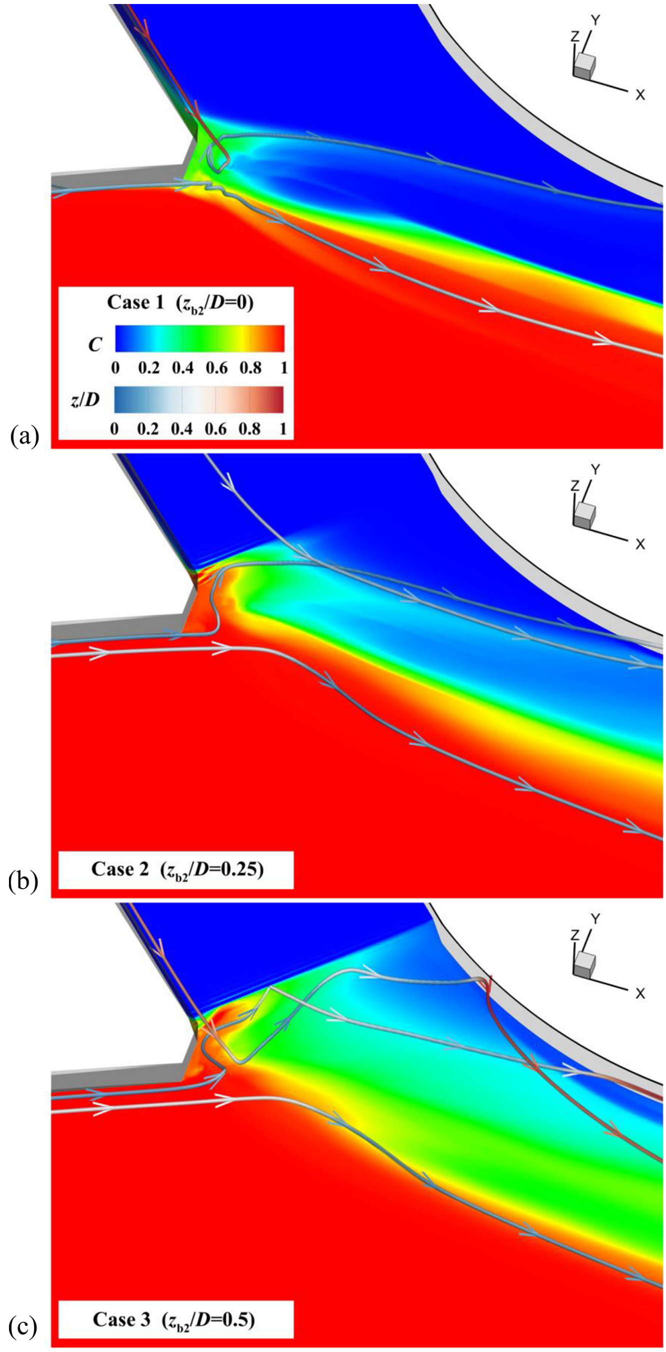

FIG. 17. Three-dimensional mean-flow stream traces launched near the confluence apex. (a) Case 1; (b) Case 2; (c) Case 3. The stream traces are colored with the elevation, z/D. The distribution of the mean concentration, C, is shown on the bottom surfaces.

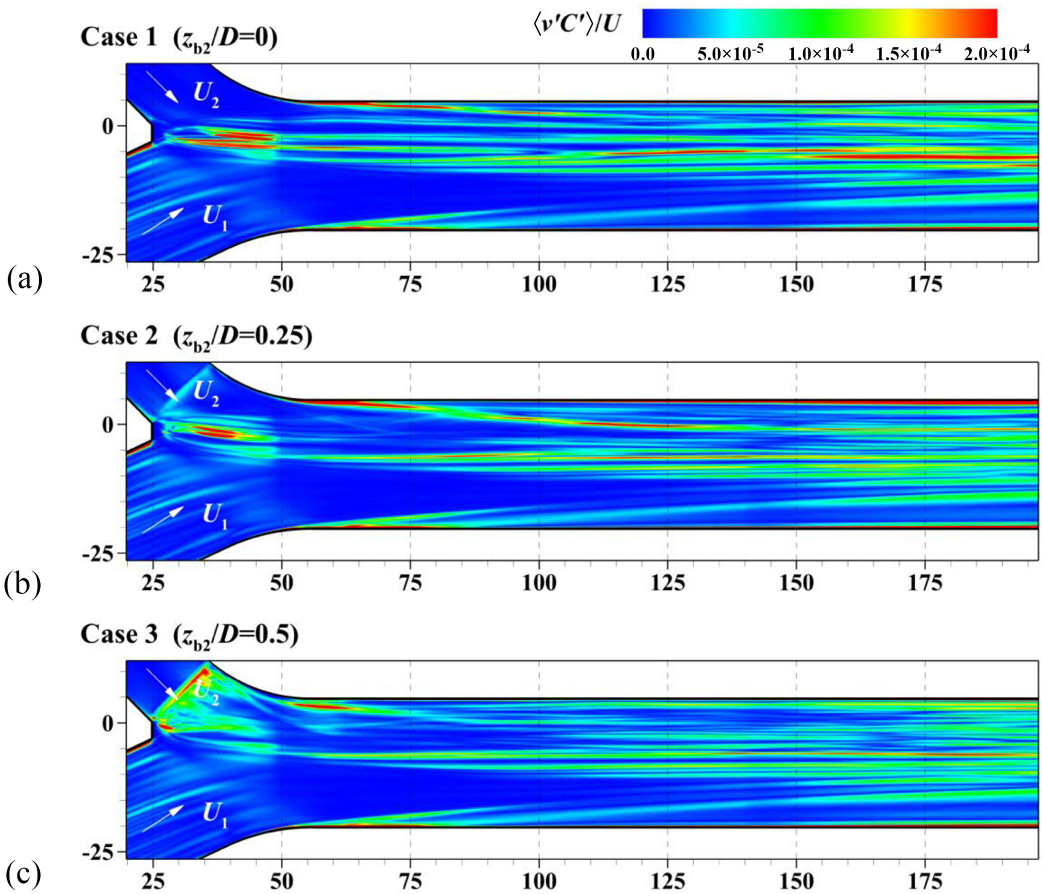

FIG. 18. Time- and depth-averaged turbulent scalar flux, $\langle C'v'\rangle/U$. (a) Case 1; (b) Case 2; (c) Case 3.

flux is the one defined with the spanwise velocity and scalar concentration fluctuations. Figure 18 compares the time- and depth-averaged distributions of the turbulent scalar flux, $\langle C'v'\rangle$, for Cases 1, 2, and 3. The two elongated regions of high $\langle C'v'\rangle$ forming starting close to the confluence apex in Case 1 are induced by the bimodal oscillations of LSV1 and RSV1 [see also discussion of Figs. 8(a) and 10(a)]. As the cores of these vortices approach the centerline of the MI, they extract mixed fluid from the cores of the vertical MI vortices. As the bed discordance increases to $z_{b2}/D = 0.25$, the bimodal oscillations of RSV1 are suppressed [Fig. 10(b)], which is why the streaks of high $\langle C'v'\rangle$ are situated on the left side of the MI in Case 2. No large amplification of $\langle C'v'\rangle$ is observed starting near the confluence apex in Case 3 where the cores of the main SOV cells are not subject to bimodal oscillations [see discussion of Fig. 10(c)]. Rather, large values of the turbulent scalar flux are observed over and downstream of the ramp in Case 3 due to eddies generated in the separated shear layer bordering the separation bubble forming downstream of the ramp [Fig. 16(c)] and the scalar penetrating inside the separation bubble from the stagnation region [see discussion of Fig 17(c)]. The distributions of $\langle C'v'\rangle$ are qualitatively similar downstream of the region where the bank lines become aligned with the streamwise direction. The regions of high $\langle C'v'\rangle$ correspond to the cores of the SOV cells and of the streamwise bank vortices (Fig. 8). Additionally, the eddies generated inside the shear layer forming at the right bank around $x/D = 60$ are the reason for the amplification of $\langle C'v'\rangle$ along the inclined streaks present on the right side of the main confluence channel.

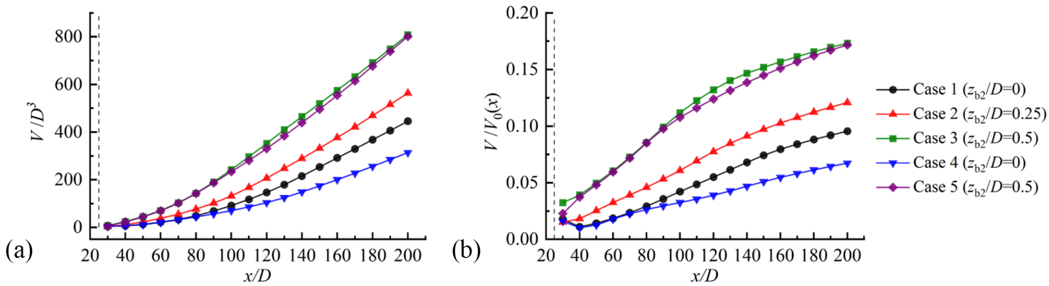

FIG. 19. Streamwise variation of the nondimensional volume of mixed fluid, V. (a) V/D^3, (b) $V/V_0(x)$. The vertical dashed line shows the location of the confluence apex.

The mixing capacity of the two joining streams can be characterized in a quantitative way by analyzing the growth of the volume of mixed fluid, V, with the distance from the confluence apex measured along the MI centerline [Fig. 19(a)]. The variable $V(x_0/D)$ is calculated by integrating C over all computational cells with $25 < x/D < x_0/D$ for which $0.1 < C < 0.9$. A second metrics quantifies the streamwise variation of the percentage of mixed fluid in between the location where the two streams come into contact ($x/D = 25$) and the current cross section. This metrics is simply calculated as $V(x/D)/V_0(x/D)$ where V_0 is the total volume of fluid in between the confluence apex and the current section [Fig. 15(b)].

Consistent with the mixing patterns in Figs. 14 and 15, V increases monotonically with increasing level of bed discordance in the three simulations performed with QR = 0.36 [Fig. 19(a)]. By $x/D = 200$, the volume of mixed fluid is by about 30% larger in Case 2 ($z_{b2}/D = 0.25$) compared to Case 1 ($z_{b2}/D = 0$). The difference increases to close to 90% for Case 3 ($z_{b2}/D = 0.5$). The increase of QR to 0.57 reduces the volume of mixed fluid by about 30% in the concordant bed case, as observed from comparing results for Case 1 and Case 4 in Fig. 19(a). Similar to what was observed for the QR = 0.36 simulations, the bed discordance increases significantly the mixing rates such that the volumes of mixed fluid are very close in the QR = 0.36 and QR = 0.57 simulations performed with $z_{b2} = 0.5$. So, the effect of increasing QR on mixing is stronger for discordant confluences. Qualitatively, the trends associated with varying QR and the level of bed discordance are the same for $V(x/D)/V_0(x/D)$ and $V(x_0/D)$. For both simulations with $z_{b2}/D = 0.5$, about 18% of the volume of water situated in between the confluence apex and $x/D = 200$ contains mixed fluid [Fig. 19(b)]. The percentage reduces to about 12% (Case 2) and 10% (Case 1) in the corresponding concordant bed simulations.

VII. BED SHEAR STRESS AND SEDIMENT ENTRAINMENT CAPACITY

This section analyses the bed shear stress magnitude in the mean flow, $\bar{\tau}$, and the root mean square of the bed shear stress magnitude, $\tau_{\rm rms}$, to describe how the capacity of the confluent flows to induce bed erosion changes with increasing bed discordance and varying QR ratio. Cheng *et al.* [52] have shown that for flows where unsteady, large-scale coherent structures are present or are advected regularly in the vicinity of the bed surface, the distributions of $\bar{\tau}$ offer an incomplete description of the sediment erosion capacity of the flow. So, one needs to also consider the variation of the instantaneous bed shear stress magnitude with respect to the mean value at a given location. This can be done by considering the probability density function (pdf) of the instantaneous bed shear stress. However, this approach is not very practical because the pdf varies from location to location. Rather, one can use $\tau_{\rm rms}$ as a first order characterization of the 'unsteadiness' of the bed shear stress at a given location with respect to the mean value [52,53]. A second objective is to analyze the role played by large-scale coherent structures in promoting erosion inside the confluence hydrodynamics zone.

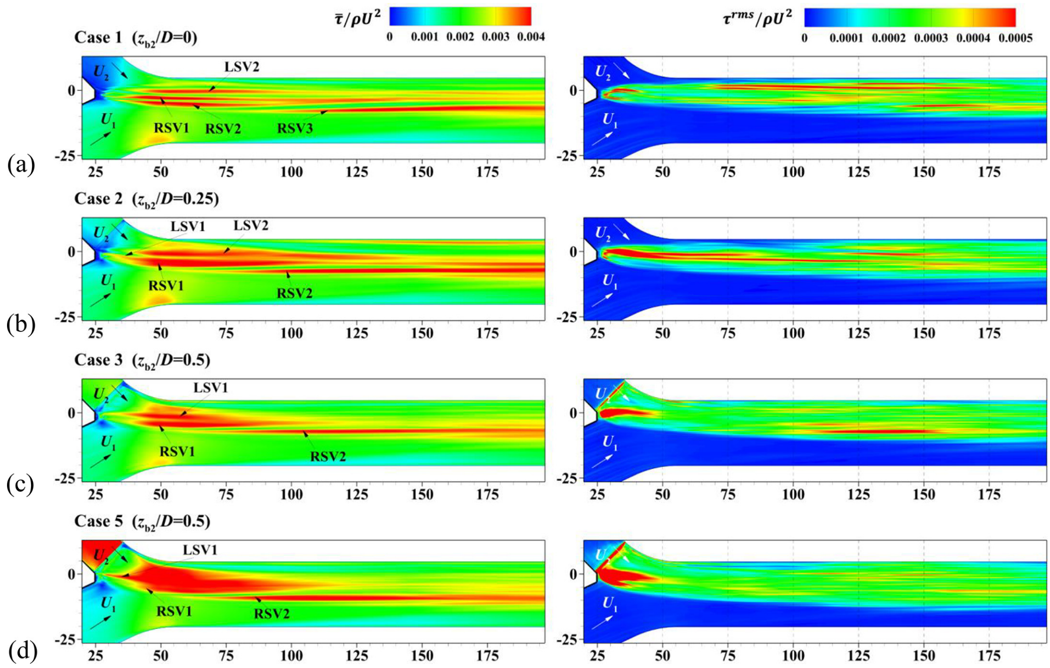

FIG. 20. Bed shear stress in the mean flow, $\bar{\tau}/\rho U^2$, (left frames) and rms of the bed shear stress fluctuations, $\tau^{\mathrm{rms}}/\rho U^2$ (right frames). (a) Case 1; (b) Case 2; (c) Case 3; (d) Case 5.

The magnitude of the local bed friction velocity in Fig. 20 is calculated as $\bar{\tau}/\rho U^2 = \frac{1}{Re}\frac{\frac{u_m}{U}}{\frac{n_1}{D}}$, where u_m is the mean velocity magnitude in a plane parallel to the bed situated at a normal distance n_1 from it and n_1 is smaller than the local thickness of the viscous sublayer. Figure 20 also includes the distributions of τ_{rms}. In the case of τ_{rms}, the mean velocity magnitude is replaced by the square root of the TKE.

Similar to the results obtained by Cheng and Constantinescu [21] for concordant confluences between very wide channels, the largest values of $\bar{\tau}$ in Case 1 [Fig. 20(a)] do not occur on the high-speed side of the MI, but rather next to the largest SOV cells, on the side where these cells advect higher streamwise velocity fluid toward the bed. In Case 1, the sediment entrainment capacity of the SOV cells is particularly high for RSV1, RSV2, RSV3, and LSV2 [see also Fig. 8(a)]. The SOV cells on the higher speed side of the confluence have the largest capacity to amplify the bed shear stress. This is consistent with findings at concordant bed confluences with natural bathymetry [9,10]. However, the fact that an SOV cell (i.e., RHS3) forming far from the confluence apex induces values of the bed shear stress values that are comparable to those generated by SOV cells forming close to the confluence apex is somewhat unexpected. Though the cores of RSV1 and LSV1 are subject to bimodal oscillations close to the confluence apex, the bed shear stresses induced by these vortices close to the confluence apex are relatively low because the two cores are situated close to the free surface. The cores get closer to the bed for $x/D > 35$. Meanwhile, the bimodal oscillations of RSV1 and LSV1 induce large values of τ_{rms} until $x/D = 40$. The weak KH mode observed in Case 1 is the main reason why the capacity of the MI vortices to increase $\bar{\tau}$ and τ_{rms} is relatively low. No clear amplification of these two quantities is observed in the region where the left-bank shear layer interacts with the MI vortices. The long streaks of high τ_{rms} in Fig. 20(a) are induced by the lateral oscillations of the SOV cells.

Compared to the concordant bed case, increasing the bed discordance height to $0.25D$ affects only quantitatively the regions of high $\bar{\tau}$. In Case 2 [Fig. 20(b)], the most coherent SOV cells

[Fig. 8(b)] on the right (RSV1, RSV2) and left side (LSV2) of the MI also contribute significantly to the increase of $\bar{\tau}$. The peak $\bar{\tau}$ values inside the elongated regions of high bed shear stress induced by RSV1 and LSV2 are larger than the corresponding peak values associated with the most coherent SOV cells in Case 1. One should also note that BV2 is also able to increase the mean bed shear stress once its core approaches the bed around $x/D = 125$. In terms of the bed shear stress fluctuations, the main qualitative change compared to Case 1 is the formation of a region of high $\tau_{\rm rms}$ in between the confluence apex and $x/D = 50$ induced by the formation and passage of more coherent KH vortices and the lateral oscillations of LSV1.

Interestingly, further increasing the bed discordance height to $0.5D$ does not result in an increase of the sediment entrainment capacity of the flow. The mechanisms responsible for the formation of the main regions of high values of $\bar{\tau}$ and $\tau_{\rm rms}$ in Case 3 [Fig. 20(c)] are essentially the same as for Case 2, with RSV1, RSV2, and LSV1 [Fig. 8(c)] being the SOV cells with the largest sediment entrainment capacity in Case 3. A secondary region of high $\bar{\tau}$ is present at the left side of LSV1 between $x/D = 45$ and $x/D = 60$. This region is induced by the core of high velocity associated with the free surface flow upstream of the ramp that plunges toward the bed once it moves past the separation bubble. However, this region does not compensate for the reduction of the size of the elongated streaks of high $\bar{\tau}$ associated with the main SOV cell and the decrease of the peak values of $\bar{\tau}$ inside these regions in Case 3 compared to Case 2. The transition from a dominant KH mode to a dominant wake mode does not result in a noticeable increase of $\tau_{\rm rms}$ beneath the upstream part of the MI in Case 3 compared to Case 2.

Comparison of the distributions of $\bar{\tau}$ and $\tau_{\rm rms}$ for Case 3 [Fig. 20(c)] and Case 5 [Fig. 20(d)] show a clear increase in the sediment entrainment capacity of the flow with increasing QR (i.e., with a larger relative discharge in the minor tributary) for a fixed value of the bed discordance height (i.e., $z_{b2} = 0.5\,D$). The increase in QR is accompanied by an important qualitative change in the distributions of the bed shear stress. The largest region of high $\bar{\tau}$ forming downstream of the confluence apex in Case 5 is not anymore associated with one of the SOV cells, but rather with the core of high-velocity free-surface fluid from the minor tributary reaching the main channel bed. So, the main mechanism for sediment entrainment is totally different on the minor tributary side of the confluence for sufficiently large values of QR. On the major tributary side, the sediment entrainment capacity of RSV1 and RSV2 slightly increases with increasing QR, meaning with decreasing discharge of the major tributary. This is explained by the movement of the MI toward the right bank in Case 5, which accelerates the flow on the right side of the MI at large distances from the confluence apex. Moreover, the strengthening of the wake mode induces a significant increase of $\tau_{\rm rms}$ beneath the upstream part of the MI in Case 5 compared to Case 3. By contrast, a mild decrease of $\tau_{\rm rms}$ is observed on both sides of the MI for $x/D > 50$.

To describe quantitatively the changes in the overall capacity of the confluent flows to entrain sediment with varying bed discordance and QR, one can compare the mean (time-averaged) flux of entrained sediment inside the main channel. The mean flux $\bar{E}$ is calculated using the instantaneous bed shear stress distributions. Van Rijn [54] pick up function is used to estimate the volumetric flux of sediment entrainment per unit time and unit area. This formula for noncohesive sediment assumes the sediment flux is proportional to $(\tau - \tau_c)^{1.5}$, where τ_c is the critical value for sediment entrainment for a given mean particle diameter, d_{50} [55]. In nondimensional form, the total instantaneous flux of sediment entrained from the bed can be expressed as

$$E(t) = \frac{1}{\rho^{1.5}U^3D^2}\int_{A'}(\tau-\tau_c)^{1.5}dA', \tag{1}$$

where $A'(t)$ is the downstream channel bed area where $\tau(t, x, y) > \tau_c$. The mean flux $\bar{E}$ is the time average of $E(t)$. Assuming $\tau_c/\tau_0 = 1.5$, where $\tau_0 = 0.0023\rho U_0^2$ is the average bed shear stress in a straight channel with the same width as that of the main channel of the confluence and fully developed flow at the same channel Reynolds number.

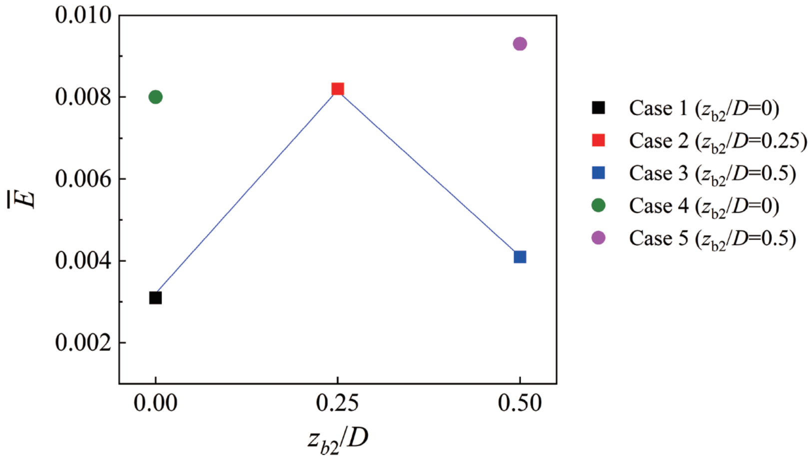

FIG. 21. Nondimensional mean (time-averaged) total volumetric flux of entrained sediment, $\bar{E}$ vs bed discordance height z_{b2}/D. The square symbols correspond to cases with $\mathrm{MR_{apex}} = 0.2$. The circle symbols correspond to cases with $\mathrm{MR_{apex}} = 0.5$. The blue line highlights that for constant $\mathrm{MR_{apex}}$, the volumetric flux of entrained sediment does not increase monotonically with increasing bed discordance height.

A main finding is that for constant QR the sediment entrainment capacity of the flow does not increase monotonically with increasing level of bed discordance (Fig. 21), which is consistent with the trends shown by the mean bed shear stress distributions in Figs. 20(a)–20(c). The mean flux $\bar{E}$ in Case 2 is more than to times higher than the values predicted for Case 1 and Case 3. The main effect of increasing QR is to increase the bed shear stresses on the minor tributary side, which explains the large increase of $\bar{E}$ with QR for constant bed discordance height (Fig. 21). In fact, in all the $\mathrm{QR} = 0.57$ simulations, the velocity ratio VR is around one, or larger than one, so the minor tributary stream has a larger erosive capacity as it enters the confluence [e.g., compare the $\bar{\tau}/\rho U^2$ distributions in Figs. 20(c) and 20(d)]. For the discordant bed cases with $\mathrm{QR} = 0.57$, the SOV cells cease to be the primary contributor to the amplification of the bed shear stresses downstream of the confluence apex.

VIII. SUMMARY AND CONCLUSIONS

The series of simulations performed as part of the present study at an asymmetrical confluence with a planform geometry close to that expected at natural confluences between a minor tributary and a larger river allowed investigating in a methodical way how the structure of the flow inside the MI, the position and coherence of the SOV cells, the rate of mixing and the sediment entrainment capacity of the flow vary with increasing bed discordance height for two different values of the discharge ratio.

The present study showed that for concordant and discordant asymmetric confluences with typical values of the aspect ratio of the channels forming the confluence, the streamwise development of the flow inside the MI is quite different from the one observed at angled concordant confluences involving very wide channels where the KH mode dominates (i.e., see Ref. [21]). In the latter case, the MI transitioned from a regime where the MI growth was driven by the merging of the vertical vortices to an intermediary one where merging was impeded and, finally, to a near-equilibrium regime where the MI vortices lost their coherence and only smaller-scale turbulence was present inside the MI. By contrast, in the present concordant confluence simulations, the growth rates of the MI over its upstream part were relatively small even when the KH mode was dominant. This low growth rates were due to two reasons. The first one is that merging between successive KH vortices did not occur. The second one is that the strong interactions of the left-bank shear layer with the MI vortices led to a very different evolution of the MI downstream of the streamwise location where the shear layer reached the MI. For such cases, there is no transition of the MI toward an equilibrium regime, similar to the one observed for shallow mixing layers. Though the shift of the MI centerline and the MI width reached a regime characterized by small rates of growth, the MI still contained strongly coherent eddies past the location where this regime started. Moreover, the main mechanism for the loss of coherence of these eddies was not the high dissipation induced by bed friction, but rather their interactions (i.e., stretching) with energetic 3D eddies on the minor tributary side of the MI.

For constant discharge ratio between the incoming flows, QR, and constant total discharge in the main channel, the increase of the bed discordance induced a gradual strengthening of the wake mode inside the MI and a decrease of the coherence of the SOV cells forming on the minor tributary side. The increase in the bed discordance height triggered an increase in the lateral shift and a decrease of the width of the MI over its downstream part, and an increase of the rates of mixing in the main channel driven by the formation of a near bed intrusion of MI fluid close to the confluence apex. Part of this mixed, near-bed fluid moved laterally close to the downstream end of the ramp where the flow depth in the minor tributary channel becomes the same as the flow depth in the main channel. This near-bed fluid was then advected downstream by the flow and eventually came into contact with the SOV cells on the minor tributary side. Once this happened, the SOV cells advected the mixed fluid laterally toward the bank line and from there toward the free surface, a process that was accompanied by strong mixing with the unmixed fluid from the minor tributary side of the main channel. Analysis of the turbulent shear stresses and primary scalar flux confirmed the important role played by both the SOV cells and the streamwise oriented vortices forming especially near the minor tributary bank line on mixing, regardless of the level of the bed discordance. The main effect of increasing the bed discordance was to damp the bimodal oscillations of the primary SOV cells, which decayed their capacity to extract mixed fluid from inside the MI, and to increase mixing near the ramp once the bed discordance level was high enough to generate a recirculation bubble.

The increase of the bed discordance led to larger velocities inside the free-surface fluid that plunges toward the bed, downstream of the region containing the bed discordance. Present results showed this is the main mechanism responsible for the increase in the sediment entrainment capacity of the flow on the minor tributary side of the main channel. Meanwhile, the decrease in the coherence of the SOV cells on the minor tributary side with increasing bed discordance weakened the main mechanism responsible for sediment entrainment at concordant confluences. The present simulations showed that for confluences with sufficiently small QR ratios, the sediment erosion potential of the flow does not vary monotonically with increasing bed discordance height. Rather, the peak value occurs for moderate levels of bed discordance. Only for sufficiently high QR values, the sediment entrainment capacity is expected to increase monotonically with increasing bed discordance height.

The findings of the present study strictly apply to high angle asymmetric confluences where a small tributary joins a larger stream. The present research approach can be extended for symmetric confluences and for small-angle confluences where bed discordance effects may be different from those observed at the type of confluences considered in the present study. Moreover, the presence of density contrast associated with differences in temperature and/or sediment loads in the two streams is expected to further increase the complexity of three-dimensional effects close to the confluence apex at discordant confluences. In particular, the lateral intrusion of MI fluid near the confluence apex promoted by bed discordance is expected to be stronger for cases where the major tributary contains heavier fluid, which should lead to increased mixing rates in the downstream channel. Such phenomena will make the object of a future study.

ACKNOWLEDGMENTS

Chenyu Jiang acknowledges funding from the National Natural Science Foundation of China (Grant No. U2340221) and the National Key R&D Program of China (Grant No.

2022YFC3202603). We gratefully acknowledge Prof. Bruce Rhoads from University of Illinois Urbana Champaign for providing the analysis that was used to choose the flow and geometrical parameters at the asymmetric confluence considered in the present study. We thank University of Iowa for providing the computational resources to run the simulations.

DATA AVAILABILITY

The data that support the findings of this article are openly available at [56].

---

[1] A. G. Roy, B. L. Rhoads, and S. P. Rice (eds.), *River Confluences, Tributaries and the Fluvial Network* (John Wiley & Sons, New York, NY, 2008).
[2] H. Herrero, M. C. Garcia, F. Pedocchi, G. Lopez, R. N. Szupiany, and C. Piacenza, Flow structure at a confluence: Experimental data and the bluff body analogy, J. Hydraul. Res. **54**, 263 (2016).
[3] G. Constantinescu and C. Gualtieri, River confluences: A review of recent field and numerical studies, Environ. Fluid Mech. **24**, 1143 (2024).
[4] B. L. Rhoads, Changes in stream channel characteristics at tributary junctions, Phys. Geogr. **8**, 346 (1987).
[5] B. L. Rhoads and S. T. Kenworthy, Flow structure at an asymmetrical stream confluence, Geomorphology **11**, 273 (1995).
[6] J. M. Gaudet and A. G. Roy, Effect of bed morphology on flow mixing length at river confluences, Nature (London) **373**, 138 (1995).
[7] G. Constantinescu, LE of shallow mixing interfaces: A review, Environ. Fluid Mech. **14**, 971 (2014).
[8] J. C. Rutherford, *River Mixing* (Wiley, Chichester, UK, 1994).
[9] G. Constantinescu, S. Miyawaki, B. Rhoads, A. Sukhodolov, and G. Kirkil, Structure of turbulent flow at a river confluence with momentum and velocity ratios close to 1: Insight provided by an eddy-resolving numerical simulation, Water Resour. Res. **47**, W05507 (2011).
[10] G. Constantinescu, S. Miyawaki, B. Rhoads, and A. Sukhodolov, Numerical analysis of the effect of momentum ratio on the dynamics and sediment-entrainment capacity of coherent flow structures at a stream confluence, J. Geophys. Res.: Earth Surf. **117**, F04028 (2012).
[11] R. D. Moser and M. M. Rogers, The three-dimensional evolution of a plane mixing layer: Pairing and transition to turbulence, J. Fluid Mech. **247**, 275 (1993).
[12] A. N. Sukhodolov, O. O. Shumilova, G. S. Constantinescu, Q. W. Lewis, and B. L. Rhoads, Mixing dynamics at river confluences governed by intermodal behavior, Nat. Geosci. **16**, 89 (2023).
[13] M. Lesieur, C. Staquet, P. Le Roy, and P. Comte, The mixing layer and its coherence examined from the point of view of two-dimensional turbulence, J. Fluid Mech. **192**, 511 (1988).
[14] V. H. Chu, Instabilities in non-rotating and rotating shallow shear flows, Environ. Fluid Mech. **14**, 1085 (2014).
[15] S. Proust, B. Cérino, C. Berni, and V. Nikora, Shallow turbulent mixing layers in open channel flows, Environ. Fluid Mech. **25**, 6 (2025).
[16] V. H. Chu and S. Babarutsi, Confinement and bed-friction effects in shallow turbulent mixing layers, J. Hydraul. Eng. **114**, 1257 (1988).
[17] S. Babarutsi and V. H. Chu, Modeling transverse mixing layer in shallow open-channel flows, J. Hydraul. Eng. **124**, 718 (1998).
[18] A. N. Sukhodolov, I. Schnauder, and W. S. J. Uijttewaal, Dynamics of shallow lateral shear layers: Experimental study in a river with a sandy bed, Water Resour. Res. **46**, W11519 (2010).
[19] Z. Cheng and G. Constantinescu, Near-field and far-field structure of shallow mixing layers, J. Fluid Mech. **904**, A21 (2020).
[20] C. Paola, When streams collide, Nature (London) **387**, 232 (1997).
[21] Z. Cheng and G. Constantinescu, Shallow mixing layers between non-parallel streams in a flat-bed wide channel, J. Fluid Mech. **916**, A41 (2021).

[22] G. Kirkil and G. Constantinescu, Effects of cylinder Reynolds number on the turbulent horseshoe vortex system and near wake of a surface-mounted circular cylinder, Phys. Fluids **27**, 075102 (2015).
[23] T. P. Lyubimova, A. P. Lepikhin, Y. N. Parshakova, V. Y. Kolchanov, C. Gualtieri, and B. Roux, A numerical study of the influence of channel-scale secondary circulation on mixing processes downstream of river junctions, Water **12**, 2969 (2020).
[24] K. F. Bradbrook, S. N. Lane, K. S. Richards, P. M. Biron, and A. G. Roy, Role of bed discordance at asymmetrical river confluences, J. Hydraul. Eng. **127**, 351 (2001).
[25] B. De Serres, A. G. Roy, P. M. Biron, and J. L. Best, Three-dimensional structure of flow at a confluence of river channels with discordant beds, Geomorphology **26**, 313 (1999).
[26] A. G. Roy and N. Bergeron, Flow and particle paths at a natural river confluence with coarse bed material, Geomorphology **3**, 99 (1990).
[27] A. Sukhodolov, J. Krick, T. Sukhodolova, Z. Cheng, B. Rhoads, and G. Constantinescu, Turbulent flow structure at a discordant river confluence: Asymmetric jet dynamics with implications for channel morphology, J. Geophys. Res.: Earth Surf. **122**, 1278 (2017).
[28] H. Tang, H. Zhang, and S. Yuan, Hydrodynamics and contaminant transport on a degraded bed at a 90-degree channel confluence, Environ. Fluid Mech. **18**, 443 (2018).
[29] S. Guillen-Ludena, A. H. Cardoso, and A. J. Schleiss, Evolution of the hydromorphodynamics of mountain river confluences for varying discharge ratios and junction angles, Geomorphology **255**, 1 (2016).
[30] A. G. Roy, R. Roy, and N. Bergeron, Hydraulic geometry and changes in flow velocity at a river confluence with coarse bed material, Earth Surf. Process. Landf. **13**, 583 (1988).
[31] J. L. Best and A. G. Roy, Mixing-layer distortion at the confluence of channels of different depth, Nature (London) **350**, 411 (1991).
[32] C. J. Boyer, A. G. Roy, and J. L. Best, Dynamics of a river channel confluence with discordant beds: Flow turbulence, bed load sediment transport, and bed morphology, J. Geophys. Res.: Earth Surf. **111**, F04007 (2006).
[33] M. Leite Ribeiro, K. Blanckaert, A. G. Roy, and A. J. Schleiss, Flow and sediment dynamics in channel confluences, J. Geophys. Res.: Earth Surf. **117**, F01035 (2012).
[34] C. L. Ramon, A. B. Hoyer, J. Armengol, J. Dolz, and F. J. Rueda, Mixing and circulation at the confluence of two rivers entering a meandering reservoir, Water Resour. Res. **49**, 1429 (2013).
[35] M. Arbat-Bofill, A. Palau, M. Sanchez-Junni, E. B. Castellet, D. Ninerola, and J. Dolz, Hydrodynamics of Ribarroja Reservoir (Ebro River, Spain): Water temperature, water velocities, and water age, in *River Flow 2014* (Taylor and Francis, London, UK, 2014).
[36] S. Guillen-Ludena, Z. Cheng, G. Constantinescu, and M. J. Franca, Hydrodynamics of mountain river confluences and its relationship to sediment transport, J. Geophys. Res.: Earth Surf. **122**, 901 (2017).
[37] Z. Cheng and G. Constantinescu, Stratification effects on flow hydrodynamics and mixing at a confluence with a highly discordant bed and a relatively low velocity ratio, Water Resour. Res. **54**, 4537 (2018).
[38] Z. Cheng and G. Constantinescu, Stratification effects on hydrodynamics and mixing at a river confluence with discordant bed, Environ. Fluid Mech. **20**, 843 (2020).
[39] P. X. Ramos, L. Schindfessel, J. P. Pêgo, and T. De Mulder, Influence of bed elevation discordance on flow patterns and head losses in an open-channel confluence, Water Sci. Eng. **12**, 235 (2019).
[40] P. X. Ramos, L. Schindfessel, J. P. Pêgo, and T. De Mulder, Flat vs. Curved rigid-lid LES computations of an open-channel confluence, J. Hydroinform. **21**, 318 (2019).
[41] O. Canelas, R. M. Ferreira, and A. Cardoso, Hydro-morphodynamics of an open-channel confluence with bed discordance at dynamic equilibrium, Water Resour. Res. **58**, e2021WR029631 (2022).
[42] B. L. Rhoads and A. N. Sukhodolov, Field investigation of three-dimensional flow structure at stream confluences: 1. Thermal mixing and time-averaged velocities, Water Resour. Res. **37**, 2393 (2001).
[43] A. D. Howard, Optimal angles of stream junction: Geometric, stability to capture, and minimum power criteria, Water Resour. Res. **7**, 863 (1971).
[44] A. G. Roy, Optimal angular geometry models of river branching, Geogr. Anal. **15**, 87 (1983).
[45] C. J. Keylock, G. Constantinescu, and R. J. Hardy, The application of computational fluid dynamics to natural river channels: Eddy resolving versus mean flow approaches, Geomorphology **179**, 1 (2012).

[46] G. S. Constantinescu, H. Pasinato, Y. Q. Wang, J. R. Forsythe, and K. D. Squires, Numerical investigations of flow past a prolate spheroid, J. of Fluids Engineering ASME **124**, 904 (2002).
[47] A. N. Sukhodolov and B. L. Rhoads, Field investigation of three-dimensional flow structure at stream confluences: 2. Turbulence, Water Resour. Res. **37**, 2411 (2001).
[48] G. Constantinescu, S. Miyawaki, B. Rhoads, and A. Sukhodolov, Influence of planform geometry and momentum ratio on thermal mixing at a stream confluence with a concordant bed, Environ. Fluid Mech. **16**, 845 (2016).
[49] K. Chang, G. Constantinescu, and S. O. Park, Assessment of predictive capabilities of detached eddy simulation to simulate flow and mass transport past open cavities, J. Fluids Eng. **129**, 1372 (2007).
[50] Y. Dubief and F. Delcayre, On coherent-vortex identification in turbulence, J. Turbul. **1**, N11 (2000).
[51] M. Koken, G. Constantinescu, and K. Blanckaert, Hydrodynamic processes, sediment erosion mechanisms, and Reynolds-number-induced scale effects in an open channel bend of strong curvature with flat bathymetry, J. Geophys. Res.: Earth Surf. **118**, 2308 (2013).
[52] Z. Cheng, M. Koken, and G. Constantinescu, Approximate methodology to account for effects of coherent structures on sediment entrainment in RANS simulations with a movable bed and applications to pier scour, Adv. Water Resour. **120**, 65 (2018).
[53] B. M. Sumer, L. H. C. Chua, N. S. Cheng, and J. Fredsøe, Influence of turbulence on bed load sediment transport, J. Hydraul. Eng. **129**, 585 (2003).
[54] L. C. Van Rijn, Sediment pick-up functions, J. Hydraul. Eng. **110**, 1494 (1984).
[55] Y. J. Chou and O. B. Fringer, A model for the simulation of coupled flow-bed form evolution in turbulent flows, J. Geophys. Res.: Oceans **115**, C10041 (2010).
[56] https://doi.org/10.25820/data.008106.